

THE VISUAL SHAPE AND MULTIPOLE MOMENTS
OF THE SUN

by

Burt Jay Beardsley

A Dissertation Submitted to the Faculty of the

DEPARTMENT OF ASTRONOMY

In Partial Fulfillment of the Requirements
For the Degree of

DOCTOR OF PHILOSOPHY

In the Graduate College

THE UNIVERSITY OF ARIZONA

1 9 8 7

INFORMATION TO USERS

The most advanced technology has been used to photograph and reproduce this manuscript from the microfilm master. UMI films the original text directly from the copy submitted. Thus, some dissertation copies are in typewriter face, while others may be from a computer printer.

In the unlikely event that the author did not send UMI a complete manuscript and there are missing pages, these will be noted. Also, if unauthorized copyrighted material had to be removed, a note will indicate the deletion.

Oversize materials (e.g., maps, drawings, charts) are reproduced by sectioning the original, beginning at the upper left-hand corner and continuing from left to right in equal sections with small overlaps. Each oversize page is available as one exposure on a standard 35 mm slide or as a 17" × 23" black and white photographic print for an additional charge.

Photographs included in the original manuscript have been reproduced xerographically in this copy. 35 mm slides or 6" × 9" black and white photographic prints are available for any photographs or illustrations appearing in this copy for an additional charge. Contact UMI directly to order.



Accessing the World's Information since 1938

300 North Zeeb Road, Ann Arbor, MI 48106-1346 USA

Order Number 8803247

The visual shape and multipole moments of the sun

Beardsley, Burt Jay, Ph.D.

The University of Arizona, 1987

U·M·I
300 N. Zeeb Rd.
Ann Arbor, MI 48106

PLEASE NOTE:

In all cases this material has been filmed in the best possible way from the available copy. Problems encountered with this document have been identified here with a check mark ✓.

1. Glossy photographs or pages _____
2. Colored illustrations, paper or print _____
3. Photographs with dark background _____
4. Illustrations are poor copy _____
5. Pages with black marks, not original copy _____
6. Print shows through as there is text on both sides of page _____
7. Indistinct, broken or small print on several pages ✓
8. Print exceeds margin requirements _____
9. Tightly bound copy with print lost in spine _____
10. Computer printout pages with indistinct print _____
11. Page(s) _____ lacking when material received, and not available from school or author.
12. Page(s) _____ seem to be missing in numbering only as text follows.
13. Two pages numbered _____. Text follows.
14. Curling and wrinkled pages _____
15. Dissertation contains pages with print at a slant, filmed as received _____
16. Other _____

University
Microfilms
International

THE VISUAL SHAPE AND MULTIPOLE MOMENTS
OF THE SUN

by

Burt Jay Beardsley

A Dissertation Submitted to the Faculty of the

DEPARTMENT OF ASTRONOMY

In Partial Fulfillment of the Requirements
For the Degree of

DOCTOR OF PHILOSOPHY

In the Graduate College

THE UNIVERSITY OF ARIZONA

1 9 8 7

THE UNIVERSITY OF ARIZONA
GRADUATE COLLEGE

As members of the Final Examination Committee, we certify that we have read
the dissertation prepared by Burt Jay Beardsley
entitled The Visual Shape and Multipole Moments of the Sun

and recommend that it be accepted as fulfilling the dissertation requirement
for the Degree of Doctor of Philosophy.

Henry Allen Hein
Raymond K. White
R. Narayan
Nirbhaj Woolf

7-27-87
Date
15 October 1987
Date
Oct. 15, 1987
Date
15 Oct 1987
Date

Date

Final approval and acceptance of this dissertation is contingent upon the
candidate's submission of the final copy of the dissertation to the Graduate
College.

I hereby certify that I have read this dissertation prepared under my
direction and recommend that it be accepted as fulfilling the dissertation
requirement.

Henry Allen Hein
Dissertation Director

7-27-87
Date

STATEMENT BY AUTHOR

This dissertation has been submitted in partial fulfillment of requirements for an advanced degree at The University of Arizona and is deposited in the University Library to be made available to borrowers under rules of the Library.

Brief quotations from this dissertation are allowable without special permission, provided that accurate acknowledgment of source is made. Requests for permission for extended quotation from or reproduction of this manuscript in whole or in part may be granted by the head of the major department or the Dean of the Graduate College when in his or her judgment the proposed use of the material is in the interests of scholarship. In all other instances, however, permission must be obtained from the author.

SIGNED: Burt Jay Beardsley

Acknowledgments

This work is the product of over 20 years effort by numerous people associated with SCLERA. The sophisticated design and operation of the telescope is proof of their ability and dedication.

In the early years of my career at SCLERA there were several people who provided instruction at the telescope and without their expertise, high quality observations would have been impossible. Drs. Thomas Caudell and Randall Bos were among those who provided this assistance. Neils Thompson also contributed a significant amount of technical support during this period. Fellow students Bill Czarnowski and Leon Yi helped collect much of the data used for this thesis. They were also responsible for the calculation of the FFTD edge location for the observations. These "lock-on points" were later converted into relative diameter measurements. Without their cooperation, work on this dissertation would have been delayed.

Several people also assisted in the preparation of this document. Don Frazier drafted the figures shown in the text. The professional help of Gigi Czarnowski and the rest of the office staff was also instrumental in the completion of this manuscript. Many constructive conversations with Paul Oglesby, Ross Rosenwald, Ron Kroll and my committee members increased the scientific value of this document. Drs. Peter Strittmatter and John Cocke, although unable to serve on my committee, provided support throughout the dissertation

process.

There is one person who requires special recognition: Henry Hill. Without his creative genius, SCLERA and this thesis would not exist. Dr. Hill's continued support through my graduate career at The University of Arizona has been the key to the success of this work. Dr. Hill sacrificed valuable time to instruct me on specialized oblateness observations at the telescope. Later, when difficulties would occur with the data analysis, he provided the insight on how best to proceed and, finally, he spent painstaking hours reviewing this manuscript. Equally important as his commitment to scientific excellence and education, is Dr. Hill's ability to create an atmosphere conducive for scientific research and cooperation that benefits everyone involved with the program.

I would also like to thank my parents, Maynard and Fern, for their encouragement from the time I first showed an interest in astronomy. Finally, I would like to thank my wonderful wife, Wendy, for her sacrifices while I pursued my career.

TABLE OF CONTENTS

	Page
LIST OF TABLES.....	vii
LIST OF ILLUSTRATIONS.....	viii
ABSTRACT.....	ix
1. HISTORICAL SIGNIFICANCE.....	1
1.1 Experimental Relativity.....	1
1.2 Variability of the Solar Oblateness.....	5
1.3 Rotating Shape Perturbations.....	7
2. RELATIONSHIP BETWEEN THE VISUAL OBLATENESS AND THE GRAVITATIONAL POTENTIAL.....	11
2.1 Von Zeipel's Theorem.....	11
2.2 Perturbation Technique.....	14
3. MEASUREMENT TECHNIQUES.....	20
3.1 The SCLERA Telescope.....	20
3.2 Solar Edge Definition.....	27
3.3 The Detectors.....	29
3.4 The Computer.....	31
4. GENERAL SOLUTION FOR DIFFERENTIAL DIAMETER MEASUREMENTS.....	34
4.1 Legendre Polynomial Description of the Solar Image.....	38
4.2 General Solution for J_2^* and J_4^*	42
5. SYSTEMATIC ERRORS INTRODUCED BY THE TELESCOPE.....	46
5.1 Optical Sources of Image Distortion.....	46
5.2 Distortions Introduced by the Servo Loop.....	48
5.3 Scan Amplitude Calibration.....	50
5.4 Detector Alignment Errors.....	52

TABLE OF CONTENTS--Continued

	page
6. OBSERVATIONS.....	56
6.1 Systematic Errors Introduced by Changes in the Limb Darkening Function.....	64
7. J_2^* AND J_4^* RESULTS.....	70
7.1 Solutions for J_4^* and J_4	72
7.2 Solutions for J_2^* and J_2	79
7.3 Atmospheric Effects.....	84
8. SOLAR PHENOMENA AND THE MULTIPOLE MOMENTS.....	86
8.1 Systematic Errors from Changes in I'	87
8.2 Solid Body Distortions of the Solar Surface.....	95
9. CONCLUSIONS.....	97
9.1 Absolute Errors from $A_1(\tilde{D})$	103
9.2 Surface Stress Contributions to the Apparent Solar Shape.....	104
9.3 Future Work.....	105
APPENDIX A	106
REFERENCES.....	113

LIST OF TABLES

Table		Page
1.	Observations used to find J_4^* and J_2^*	71
2.	Least Squares Coefficients for J_4^*	75
3.	Least Squares Coefficients for J_2^*	81
4.	Values of the Brightness Coefficients $R_{h,i,j}^4$	91
5.	Values of the Brightness Coefficients $R_{h,i,j}^2$	91
6.	J_4^* and J_4 Results.....	98
7.	J_2^* and J_2 Results.....	99
8.	Summary of Efforts to Determine J_2	101

LIST OF ILLUSTRATIONS

Figure		Page
1.	Cross Section of Telescope and Building.....	21
2.	The Solar Image Plane.....	23
3.	Mangin Tracking Optics.....	24
4.	Celestial Coordinate System.....	36
5.	$D_{m,n}(-\theta, 21.5)$ Vs. Time for Day Number 180.....	57
6.	$\bar{D}_{m,n}(21.5)$ Vs. Time for Day Number 180.....	61
7.	$D_{m,n}(-\theta, a_1) - D_{m,n}(-\theta, a_4)$ vs. Time for Day Number 171.....	62
8.	$\bar{A}_1(\bar{D})$ Vs. N.....	74
9.	$\bar{A}_1(\Delta D)$ Vs. N.....	80
10.	$R^4_{h,4,1}$ Vs. Scan Amplitude.....	92
11.	$R^2_{h,4,1}$ Vs. Scan Amplitude.....	92

ABSTRACT

This thesis describes the 1983 solar shape investigation performed at the Santa Catalina Laboratory for Experimental Relativity by Astrometry (SCLERA). Solar diameter measurements, with the North Solar Pole defined as $\theta = 0^\circ$ polar angle, have been made between the following polar coordinates: from $\theta = 0^\circ$ to $\theta = 180^\circ$ (the polar diameter), from $\theta = 90^\circ$ to $\theta = -90^\circ$ (the equatorial diameter), from $\theta = -45^\circ$ to $\theta = 135^\circ$ and from $\theta = 45^\circ$ to $\theta = -135^\circ$. Expressing the Sun's apparent shape in terms of a Legendre series, these diameters have enabled the calculation of the P_2 (quadrupole) and P_4 (hexadecapole) shape coefficients.

The theoretical framework used to provide a relationship between the observed shape of the Sun and the multipole moments of the solar gravitational potential field has been improved to include, in general, the effect of differential rotation in both latitude and radius. Using the shape coefficients and the theoretical framework, the gravitational potential multipole moments, expressed as the P_2 and P_4 coefficients of a Legendre series, have been found to be $J_2 = (3.4 \pm 1.3)E-6$ and $J_4 = (1.7 \pm 1.1)E-6$, respectively. It has been found that the contribution to the perihelion precession of Mercury's orbit, caused by the combined effects from the gravitational quadrupole term and general relativity, was approximately 1% different from the observed amount after all other known Newtonian contributions had been

removed from the observed precession.

The total apparent oblateness ΔR (equator-polar radii) found from SCLERA observations is $\Delta R = 13.8 \pm 1.3$ milliarcseconds. The surface rotation contribution $\Delta R'$ to the apparent solar shape is $\Delta R' = 7.9$ milliarcseconds. The quoted uncertainties represent formal statistical 1σ errors only.

Also, it has been shown that large changes in the apparent limb darkening functions were occurring near the equatorial regions of the Sun during the time of the observations.

Evidence for periodic shape distortions near the equator have also been found.

CHAPTER 1

HISTORICAL SIGNIFICANCE

The shape of the Sun has been under investigation for 2 1/2 centuries (see Stebbins 1975 for a review of the early work in the field). However, the modern era of oblateness research began with the construction of a solar heliometer at Princeton University by Robert Dicke, Mark Goldenberg and Henry Hill in 1963. The purpose of the telescope was to measure the apparent solar oblateness and through theoretical considerations infer a gravitational quadrupole moment for the Sun. This latter quantity was originally of interest because of its importance to experimental relativity.

1.1 Experimental Relativity

The potential field associated with the mass quadrupole moment of the Sun creates principally a Newtonian perturbation on the orbit of the planets such that their perihelia are precessed. Since the perturbing potential $\propto 1/r^3$ (see equation 2.1.7), the precession for Mercury's orbit is greatest and consequently most easily detected. Unfortunately, general relativistic precession of the perihelia is very difficult to decouple observationally from the precession caused from the quadrupole moment.

The equation for the perihelion advance for Mercury including relativistic and solar quadrupole moment terms is:

$$\Delta\omega = 42.95 \left[\frac{1}{3}(2 + 2\gamma - \beta) + 0.029 J_2 \times 10^5 \right] \quad 1.1.1$$

where J_2 is a dimensionless parameter describing the magnitude of the quadrupole moment of the Sun and is defined in equation 2.1.7. $\Delta\omega$ represents the observed perihelion advance in arcseconds per century (arcsec c^{-1}) from oblateness or relativistic contributions, and γ and β represent parameters describing the theory of gravitation assumed in the parameterized post Newtonian (PPN) formalism. For general relativity (GR) these parameters are both unity. There are other PPN parameters associated with this equation however, for conservative theories of gravitation, they are normally assumed to be zero¹.

Equation 1.1.1 shows that an independent measure of the contribution of the solar quadrupole moment to the precession is needed so various gravitational theory predictions can be compared with observations. This comparison between observation and theory represents one of Einstein's classical tests of relativity (Einstein 1916).

The first modern measurements of the solar oblateness were obtained in 1966 and the preliminary result was $\Delta R = 48 \pm 2$ milliarcseconds (Dicke and Goldenberg 1967) where ΔR represents the difference in radius between the equator and pole. After numerous re-analyses of the data, a value of $\Delta R = 42 \pm 2$ milliarcseconds was found (Dicke 1981).

1. For a complete review of the PPN formalism see Will (1981) and for the current status of experimental relativity see Will (1984, 1986).

An oblateness this large results in a value of $\Delta\omega \approx 47 \text{ arcsec } c^{-1}$ if $\gamma = \beta = 1$ as required by GR. This is about $4 \text{ arcsec } c^{-1}$ in excess of what is observed after other solar system perturbations have been removed. Theories such as the Brans-Dicke (1961) scalar tensor theory with adjustable scaling parameters are favored by this result instead of GR.

In 1972, when Dicke was re-analyzing the 1966 observations, he found that there was an unexpected periodicity in his residuals that was later determined to be a 12.38 sidereal day solar oscillation (Dicke 1978, 1981). The oscillation was interpreted, in one model, as a decoupled rapidly rotating solar core (see Dicke 1982 and references therein) or in a second model, as a rotating toroidal magnetic field. Because of these results, although controversial, the study of the solar shape became important not only for use in experimental relativity but as a probe of the solar interior.

In the mid 1960's, H. Hill moved to Wesleyan University where he and student Carl Zanoni decided to design a telescope, based on the experience gained at Princeton, that would be capable of measuring the gravitational deflection of starlight passing near the limb of the Sun. The site selection was in the Santa Catalina Mountains near Tucson Arizona and the telescope was completed in 1970.

As an extension of the deflection of starlight experiment, which required an accurate angular diameter of the Sun to be measured,

the SCLERA¹ oblateness program developed in the early 1970's. An important result of the early 1970's was that extreme care must be exercised in relating an observed visual solar oblateness to intrinsic solar oblateness. An edge definition was developed that had high sensitivity to changes in the limb darkening function. The technique could distinguish between an actual diameter change and an apparent diameter change resulting from a variation in limb darkening functions between polar angles. This definition had the additional advantage of having low sensitivity to atmospheric seeing fluctuations.

Hill and Stebbins (1975a) with the use of the edge definition derived a value of $\Delta R = 9.2 \pm 6.3$ milliarcseconds, which resulted in a small value for the solar gravitational quadrupole moment. Using their quadrupole term, the observed non-Newtonian precession of Mercury's orbit was then in very good agreement with the prediction from GR. The data set was not temporally long enough to determine if a 12.38 day period existed in the data.

Hill, Stebbins, and Brown (1976) also showed that the results of Dicke and Goldenberg (1967, 1974) could be significantly influenced by several classes of variations in limb darkening functions that had been proposed in the early 1970's as plausible models. These models produced a false oblateness that was detectable with SCLERA-type observations.

1. SCLERA is an acronym for the Santa Catalina Laboratory for Experimental Relativity by Astrometry, a facility jointly owned and operated by the University of Arizona and Wesleyan University.

The conclusions from Hill, Stebbins, and Brown (1976) were also supported by work done by Chapman and Klabunde (1982). They analyzed the solar facular contribution to a false oblateness signal that would result from Princeton type measurements and came to the conclusion that a significant portion of the 1966 Princeton measurements could be caused by the contamination of solar faculae.

1.2 Variability of the Solar Oblateness

In the 1980's, oblateness work was continued using both Princeton and SCLERA-type observations. However, the Princeton telescope was moved from Princeton to Mt. Wilson in California for better observing conditions.

Princeton-type solar observations were made in 1983, 1984, and 1985 (Dicke, Kuhn, and Libbrecht 1985, 1986, 1987). They found values of $\Delta R = 18.2 \pm 1.4^1$, 5.6 ± 1.3 , and 14.6 ± 2.2 milliarcseconds for 1983, 1984 and 1985 respectively. These results and the analysis of the 1966 data led to their suggestion that the intrinsic oblateness may be varying with the 22 year solar magnetic cycle. There was marginal evidence for the 12.38 day sidereal period oscillation in 1983 and 1985, but no evidence for it in 1984.

Hill and Beardsley (1987) re-examined the published observational results and demonstrated that, statistically, the limb darkening function was different along orthogonal diameters for the

1. The ΔR shown for the 1983 results includes a ~ 1 milliarcsecond systematic correction described in Dicke *et al.* (1986): There is also another solution to the 1983 data set that is listed in chapter 9 and table 8.

1983, 1984, and 1985 data sets of Dicke, Kuhn and Libbrecht (1985, 1986, and 1987). Also the form of the variations in the limb darkening functions changed every year. This result along with several other tests led Hill and Beardsley (1987) to the conclusion that a significant false oblateness due to the limb darkening function differences could remain in the results of Dicke, Kuhn and Libbrecht (1985, 1986, and 1987). The possibility for systematic error introduced by these differences considerably weakens the basis of the suggestion that the intrinsic oblateness (or surfaces of constant potential) may be varying with the solar cycle.

The oblateness work at SCLERA in the 1970's led to the discovery of global solar oscillations (Hill and Stebbins 1975b) and subsequent work at SCLERA has made significant contributions to the field of solar seismology since that time¹. In an unexpected development, it was discovered that the perturbation to the gravitational potential field could be inferred from an internal rotation curve derived from measurements based on the fine structure splitting of multiplets found in the global oscillations. This created a potentially very powerful probe of the solar interior. Since that time numerous groups have identified multiplet splittings and have made estimates of the internal rotation curve [see Hill, Bos and Goode (1982), Hill (1984, 1985a,b), Hill, Rabaey, and Rosenwald (1986), and Hill, Rabaey, Yakowitz, and Rosenwald (1986) for SCLERA results; Duvall and Harvey (1984), Brown (1985), and Libbrecht and Zirin (1986) for a

1. For a review of solar seismology work done at SCLERA see Hill and Rosenwald (1986).

second; and Duvall, Harvey, and Pomerantz (1986) for a third]. The first group of findings are from differential radius observations at SCLERA based on longer period oscillations, the second group is based on the Doppler shift observations of the five minute oscillations, and the third set of findings is based on intensity observations within an absorption line of the five minute oscillations.

Unfortunately, there is much disagreement between the rotation curves derived from these groups creating uncertainty in the rotational contribution to the solar quadrupole moment. Even when the differences in these results are resolved, the study of the visual solar oblateness will be important because it is currently the only available technique for deriving the external gravitational potential field from all stresses altering the internal mass distribution of the Sun. The J_2 derived from multiplet splitting is primarily a measure of the dynamical contribution.

1.3 Rotating Shape Perturbations

Hill and Czarnowski (1987) found that 16 frequencies originally classified as gravity modes by Delache and Scherrer (1983), based on 1979 differential velocity observations, were harmonics of a fundamental synodic frequency $\nu_0 = 0.4447 \pm 0.0004 \mu\text{Hz}$. A harmonic structure was also reported by Hill and Czarnowski (1987) in the differential velocity observations of Kotov et al. (1983) with a fundamental frequency of $\nu_0 = 0.4452 \pm 0.0005 \mu\text{Hz}$. A similar harmonic structure was found in the SCLERA differential radius observations with

$\nu_0 = 0.4447 \pm 0.0020$ μHz . The signals in each of the three cases were consistent with a rotating localized perturbation. However, the average fundamental frequency corresponds to $1/(25.960 \pm 0.021)$ of the average 1/day sideband frequency appropriate to the season in which the observations were made and as a result could be artifacts of the data windows used for the observations.

Claverie et al. (1982) also reported finding a synodic frequency of $\nu = 0.884 \pm 0.007$ μHz using whole disk velocity observations, nearly twice the fundamental frequency found above. Dicke (1983) re-analyzed the Claverie et al. observations and derived a value of $\nu = 0.9035 \pm 0.0071$ μHz , almost in exact agreement with Dicke's result from the 1966 oblateness data. This supported Dicke's suggestion of a rapidly rotating magnetic core. However, the whole disk measurements had significant contamination from sunspots, which may have affected the results (Anderson and Maltby 1983).

The magnetic field needed to support the observed surface distortion for the 1966 oblateness observations (Dicke 1976) was found to be $\sim 10^8$ G. This large amplitude rotating toroidal field was in disagreement with the upper limits of $\sim 3 \times 10^6$ G placed on the internal magnetic field from theoretical work by Dziembowski and Goode (1983). Their results were based on fine structure splitting due to magnetic fields. The analysis was done using differential radius data obtained from Hill, Bos, and Goode (1982).

Hill and Czarnowski (1987) found that the average value of the first harmonic from the three cases they investigated differed by only

1.9 σ from the $\nu = 0.903 \pm 0.0071$ μHz synodic frequency found by Dicke for his 1966 oblateness data. If Dicke and Claverie observed the first harmonic and not the fundamental frequency as Hill and Czarnowski asserted, then they have measured a surface distortion which was rotating 4.1% faster than the equatorial rotation rate of sunspots.

Both interpretations, a core rotating at twice the surface rate, as suggested by Dicke, or a perturbation rotating at slightly more than the surface sunspot rate, as suggested by Hill and Czarnowski, would be difficult to reconcile with internal rotation curves derived from either Doppler shift observations or the findings based on intensity observations within an absorption line. These two observational techniques have found the internal rotation to be approximately constant.

The rotation curve based on differential radius observations predicts that the surface perturbations are originating at a depth of 2% of the solar radius if ν_0 found above is the fundamental frequency. If the frequency found by Claverie et al. (1982) analyzing whole disk observations and by Dicke (1983) analyzing 1966 oblateness data is a fundamental frequency, and the differential radius rotation curve is assumed, then the perturbation would be occurring at a depth of about 0.2 to 0.3 solar radii. The distortion could be associated with the base of the convection zone.

Clearly, the confused state of our current observational knowledge concerning the static and dynamical nature of the Sun needs

to be further investigated both through the use of the observed multiplet splitting and observations of the visual shape.

In this thesis are described the results of the SCLERA program for determining the solar shape and a preliminary search for periodic surface distortions from observational data obtained during the summer of 1983. A general theoretical framework is also developed to relate a surface of constant gravitational potential to the apparent solar shape. It is found that the work done by Dicke (1970) is unnecessarily restrictive in the types of surface stresses that can be related to an apparent oblateness. These surface stresses alter the apparent shape of the Sun such that surfaces of constant potential as defined by the mass distribution do not correspond with the observed shape of the Sun.

The theoretical framework developed in chapter 2 also allows the calculation of surface stress contributions to higher order multipole moment shape terms used to describe the solar profile. The observations were made in such a way as to utilize this formalism so both quadrupole and hexadecapole shape terms determined from the observations could be related to the corresponding multipole moments for the gravitational potential field.

CHAPTER 2

RELATIONSHIP BETWEEN THE VISUAL OBLATENESS AND THE GRAVITATIONAL POTENTIAL

2.1 Von Zeipel's Theorem

The Sun's visual oblateness and gravitational potential have been traditionally related by use of Von Zeipel's Theorem (Von Zeipel 1924, Dicke 1970, Libbrecht 1984). This theorem states that if there are no surface stresses, such as those which may be introduced by velocity or magnetic fields, then surfaces of constant P (pressure), ρ (density), T (temperature), and ϕ (gravitational potential) all coincide and the apparent oblateness is a surface of constant gravitational potential. This can be shown by first assuming hydrostatic equilibrium:

$$\nabla P + \rho \nabla \phi = 0 \quad . \quad 2.1.1$$

The curl of this equation is

$$\nabla \rho \times \nabla \phi = 0 \quad 2.1.2$$

so that the normals to surfaces of constant ρ and ϕ point in the same direction and as a consequence, the surfaces of constant ρ and ϕ coincide. Using the perfect gas equation of state (with constant

chemical composition) and the result expressed in equation 2.1.2, it is found that surfaces of constant ρ , P , T , and ϕ all coincide. An important consequence of Von Zeipel's Theorem is that any interior source of distortion in the gravitational field at the surface will manifest itself as a shape change in the surface layers of the Sun. Thus, measuring the shape of the surface layers is equivalent to measuring surfaces of constant gravitational potential.

Since surface rotation and magnetic fields can introduce stresses at the surface of the Sun, deviations from Von Zeipel's Theorem will occur. Von Zeipel's relationship can be generalized to relate the apparent surface to a constant potential surface in the restrictive case where the source of a surface distortion can be expressed as ρ times the gradient of a scalar potential. For example, if equation 2.1.1 derived from the momentum equation is modified to include surface rotation we find:

$$\nabla P + \rho \nabla \phi = \rho \Omega^2 r \sin \theta (\sin \theta \hat{r} + r \cos \theta \hat{\theta}) , \quad 2.1.3$$

where r is the radial coordinate and θ is the polar angle of a spherical polar coordinate system. The polar unit vectors associated with r and θ are \hat{r} and $\hat{\theta}$, respectively. The positive direction is defined outward and the North Solar Pole is defined as $\theta = 0^\circ$ in a right handed coordinate system. If $\Omega(r, \theta)$, the angular rotation rate of the Sun, is such that the resulting acceleration components can be expressed as a gradient of a scalar, $\nabla \psi$, then equation 2.1.3 becomes:

$$\nabla P + \rho \nabla(\phi + \psi) = 0 \quad . \quad 2.1.4$$

Also,

$$\nabla \rho \times \nabla(\phi + \psi) = 0 \quad . \quad 2.1.5$$

As a consequence, normals to surfaces of constant P , ρ , and T are in the same direction as normals to surfaces of constant $(\phi + \psi)$. Two examples of $\Omega(r, \theta)$ which result in surface accelerations expressible as gradients of scalar fields, and which have been used in solar oblateness studies, are rigid rotation and uniform rotation on cylinders.

For the example of a rigidly rotating Sun with $\Omega(r, \theta)$ equal to a constant, ω_0 , Dicke (1970) found,

$$\Delta R/R = (3/2) J_2 + (1/2) \omega_0^2 R/g \quad , \quad 2.1.6$$

where ΔR is the apparent equator - pole oblateness, R is the mean radius of the Sun and g is the surface gravity. J_2 is related to ϕ by:

$$\phi(r, \theta, \phi) = - \frac{GM_0}{r} \left[1 - \sum_{\ell=2}^{\infty} \left(\frac{R}{r} \right)^{\ell} J_{\ell} P_{\ell}(\cos \theta) \right] , \quad r > R \quad 2.1.7$$

where G is the gravitational constant, M_0 is the mass of the Sun and P_{ℓ} is the Legendre polynomial of degree ℓ . Assuming the Sun's $\Omega(r, \theta)$ is a

linear combination of the two special cases noted above, Dicke (1970) used $\Omega(r, \theta) = \omega_0 + (\omega_1 r \sin \theta)/R$, with $\omega_0 = 1.66 \times 10^{-6}$ and $\omega_1 = 1.20 \times 10^{-6} \text{ rad sec}^{-1}$, to find that the rocation term contributes about 8.1×10^{-6} to $\Delta R/R$. For this assumed $\Omega(r, \theta)$, the surfaces of constant $\phi + \psi$, ρ , P , and T all coincide since the perturbing force could be expressed as ρ times the gradient of a scalar ψ . However, there is no experimental support for assuming this form for $\Omega(r, \theta)$ and, as a consequence, there may be non-negligible corrections that must be made to the $\Delta R/R$ that Dicke obtained.

Although there is disagreement on internal rotation of the Sun, most work indicates that the Sun rotates very differently than either of the two rotation curves assumed by Dicke (see references listed in Chapter 1). Furthermore, the effect of other surface stresses which cannot be written in terms of a gradient of a scalar, cannot be conveniently calculated.

2.2 Perturbation Technique

A more general relationship can be derived by perturbing the momentum equation. From Unno et al. (1979):

$$\frac{1}{\rho} \nabla_{\perp} P' + \nabla_{\perp} \phi' = \frac{f_{\theta}'}{\rho} \hat{\theta} \quad 2.2.1$$

where the transverse gradient, ∇_{\perp} , is defined by:

$$\nabla_{\perp} = \frac{\hat{\theta}}{r} \frac{\partial}{\partial \theta} + \frac{1}{r} \frac{\hat{\phi}}{\sin \theta} \frac{\partial}{\partial \phi} \quad , \quad 2.2.2$$

and P' , ϕ' , and f'_θ represent Eulerian perturbations in the pressure, gravitational potential and the $\hat{\theta}$ component of the surface stress, respectively. By taking the divergence of equation 2.2.1, it is found that

$$\nabla_\theta^2 \left(\frac{P'}{\rho} + \phi' \right) = \frac{1}{r \sin \theta} \frac{\partial [\sin \theta (f'_\theta / \rho)]}{\partial \theta} \quad . \quad 2.2.3$$

This equation can be evaluated by expressing $(\frac{P'}{\rho} + \phi')$ in a Legendre series and solving for the coefficients. Let

$$\frac{P'}{\rho} + \phi' = \sum a_\ell P_\ell \quad 2.2.4$$

with $a_\ell(r)$ representing the Legendre coefficients. Notice that in general these coefficients are a function of the radial coordinate since the perturbations are depth dependent. Using the property

$$\nabla_\theta^2 P_\ell = - \frac{\ell(\ell+1)}{r^2} P_\ell \quad 2.2.5$$

and the orthogonality of the polynomials, the coefficients are found to be

$$a_\ell(r) = \frac{-(2\ell+1)r}{2\ell(\ell+1)} \int_0^\pi P_\ell \frac{\partial(\sin \theta f'_\theta / \rho)}{\partial \theta} d\theta \quad . \quad 2.2.6$$

Next, it is necessary to relate the Eulerian perturbations

$(\frac{P'}{\rho} + \phi')$ to a displacement $\Delta r_{\phi,p}$ between surfaces of constant ϕ and P . First, consider the two surfaces of constant ϕ that exist before and after perturbing. In first-order perturbations, the perturbed surface is displaced from the original by Δr_{ϕ} , where

$$\Delta\phi = 0 = \phi' + \frac{\partial\phi}{\partial r} \Delta r_{\phi} = \phi' - g \Delta r_{\phi} \quad 2.2.7$$

or,

$$\Delta r_{\phi} = \frac{\phi'}{g} . \quad 2.2.8$$

Similarly, the displacement between the two surfaces of constant pressure is

$$\Delta P = 0 = P' + \frac{\partial P}{\partial r} (\Delta r_{\phi} - \Delta r_{\phi,p}) . \quad 2.2.9$$

Therefore, from equations 2.2.8 and 2.2.9

$$\Delta r_{\phi,p} = \frac{1}{g} \left(\frac{P'}{\rho} + \phi' \right) \quad 2.2.10$$

where $\Delta r_{\phi,p} = \Delta r_{\phi} - \Delta r_p$ is the displacement between the perturbed potential surface and the perturbed pressure surface. Substituting equation 2.2.4 into 2.2.10, we find

$$\Delta r_{\phi,p} = \frac{1}{g} \sum a_{\ell} P_{\ell} . \quad 2.2.11$$

Therefore, the separation between a surface of constant potential and a surface of constant pressure can be calculated using this formalism for any known surface stress (for which $\phi'/\phi \ll 1$) in terms of the a_ℓ and Legendre polynomials. This relationship was derived without any knowledge of $f'_r \hat{r}$. Consequently, detailed knowledge of the internal properties of the Sun, such as rotation or magnetic fields, was unnecessary in solving for $\Delta r_{\phi,p}$.

Appendix A shows that to a very good approximation,

$\Delta r_T = \Delta r_\rho = \Delta r_p$ where Δr_T and Δr_ρ are defined analogously to Δr_p for temperature and density, respectively. Since these three surfaces coincide, the difference between the apparent shape and an equipotential surface is found by equation 2.2.11.

The relationship between the observed oblateness and ϕ can now be expressed as

$$\Delta R/R = - \sum_{\ell=2}^{\infty} (J_\ell + J'_\ell) \Delta P_\ell, \quad 2.2.12$$

where ΔR represents the difference in solar radius at any two solar polar angles. J_ℓ are the Legendre coefficients found in equation 2.1.7 used in describing ϕ , the coefficients $J'_\ell = [a_\ell(R)]/(gR)$ represent the surface stress contributions to $\Delta R/R$, and the ΔP_ℓ are differences in Legendre polynomials associated with the two solar polar angles for a given ℓ .

A perturbing force that is well observed at the solar surface is differential rotation. The $\hat{\theta}$ component in equation 2.2.1 for

surface rotation is $f'_1/\rho = \Omega^2(R, \theta) R \sin \theta \cos \theta \hat{\theta}$. Snodgrass (1983) derives expressions for Ω that have been based on either Doppler techniques or magnetic field rotation. Observations taken by SCLERA near the limb of the Sun penetrate to a depth of about $\tau = 0.1$ at a wavelength of 0.5μ . The radiation responsible for the absorption lines, used by the Doppler measurements, originate much higher in the photosphere while the magnetic fields associated with the sunspots probably originate at depths greater than $\tau = 0.1$. Thus, the proper rotation curve for SCLERA-type observations should be intermediate between the curve found from Doppler measurements and the curve found from magnetic fields. In the following analysis, coefficients based on surface rotation of magnetic fields are used. However, if the Doppler based coefficients are adopted, the rotation contribution to ΔR would be modified by ≈ 0.1 milliarcsecond. Expressing the coefficients obtained from Snodgrass (1983) in the following Legendre series,

$$\Omega = \sum_{\ell=0}^2 \Omega_{2\ell} P_{2\ell} \quad , \quad 2.2.13$$

it is found that the coefficients based on the rotation of magnetic fields are: $\Omega_0 = 2.670 \pm 0.006$, $\Omega_2 = -0.515 \pm 0.016$, and $\Omega_4 = -0.099 \pm 0.005$ ($\times 10^{-6} \text{ rad sec}^{-1}$). Equations 2.2.6 and 2.2.13 can be used to evaluate a_2 and a_4 :

$$a_2 = r^2 \left(\frac{1}{3} \Omega_0^2 + \frac{2}{21} \Omega_0 \Omega_2 + \frac{1}{21} \Omega_2^2 - \frac{8}{63} \Omega_0 \Omega_4 - \frac{4}{693} \Omega_2 \Omega_4 + \frac{81241}{48048} \Omega_4^2 \right), \quad 2.2.14$$

and,

$$a_4 = r^2 \left(\frac{6}{35} \Omega_0 \Omega_2 + \frac{12}{385} \Omega_2^2 + \frac{2}{77} \Omega_0 \Omega_4 + \frac{8}{455} \Omega_2 \Omega_4 + \frac{6}{1001} \Omega_4^2 \right) \quad . \quad 2.2.15$$

Substituting the magnetic field rotation coefficients into these two equations and using equation 2.2.11,

$$J_2' = 5.82 \times 10^{-6} \quad 2.2.16$$

and

$$J_4' = -0.59 \times 10^{-6} \quad 2.2.17$$

where $J_2' = a_2/gR$ and $J_4' = a_4/gR$. These results indicate an equatorial to polar distortion of

$$[\Delta r_p(\text{eq}) - \Delta r_p(\text{pole})]/R = 8.36 \times 10^{-6}.$$

Dicke (1970) and Libbrecht (1984) have argued on theoretical grounds that other magnetic, viscosity, or velocity stress fields must have a negligible contribution to Δr . However, changes in the limb darkening functions between the equator and pole which result in a false evaluation of oblateness, have been well documented (Hill and Stebbins 1975, Hill and Beardsley 1987). Although the mechanism causing this phenomenon is not understood, the effects on Δr_p , Δr_T , and Δr_ρ must be addressed. This problem will be discussed in later chapters.

CHAPTER 3

MEASUREMENT TECHNIQUES

3.1 The SCLERA Telescope

The SCLERA telescope, located near the top of Mt. Bigelow in the Santa Catalina Mountains, has been described in numerous documents (Zanoni 1966, Clayton 1973, Oleson et al. 1974, Patz 1975, and Stebbins 1975). Only a general description of it shall be given here. In figure 1 (taken from Stebbins 1975) the optical and mechanical components are shown. The telescope is a Schupmann medial elevation-azimuth design, with a 12.5 cm f/100 objective, and color-correcting, folded, Mangin optics.

Sunlight enters through a window that is attached to an outer cylinder. The window and outer cylinder can be rotated in elevation and are located on the side of the dome at the top of the tower. After passing through the window, sunlight is directed horizontally by a mirror, M_1 , toward the center of the tower inside the dome. The outer cylinder and window provide protection for this mirror. M_1 is fixed relative to an inner cylinder that can also be rotated in elevation. A second mirror, M_2 , receives the sunlight from M_1 and directs the light downward through the objective. The objective, M_2 and the inner cylinder attached to M_1 are all supported by a table.

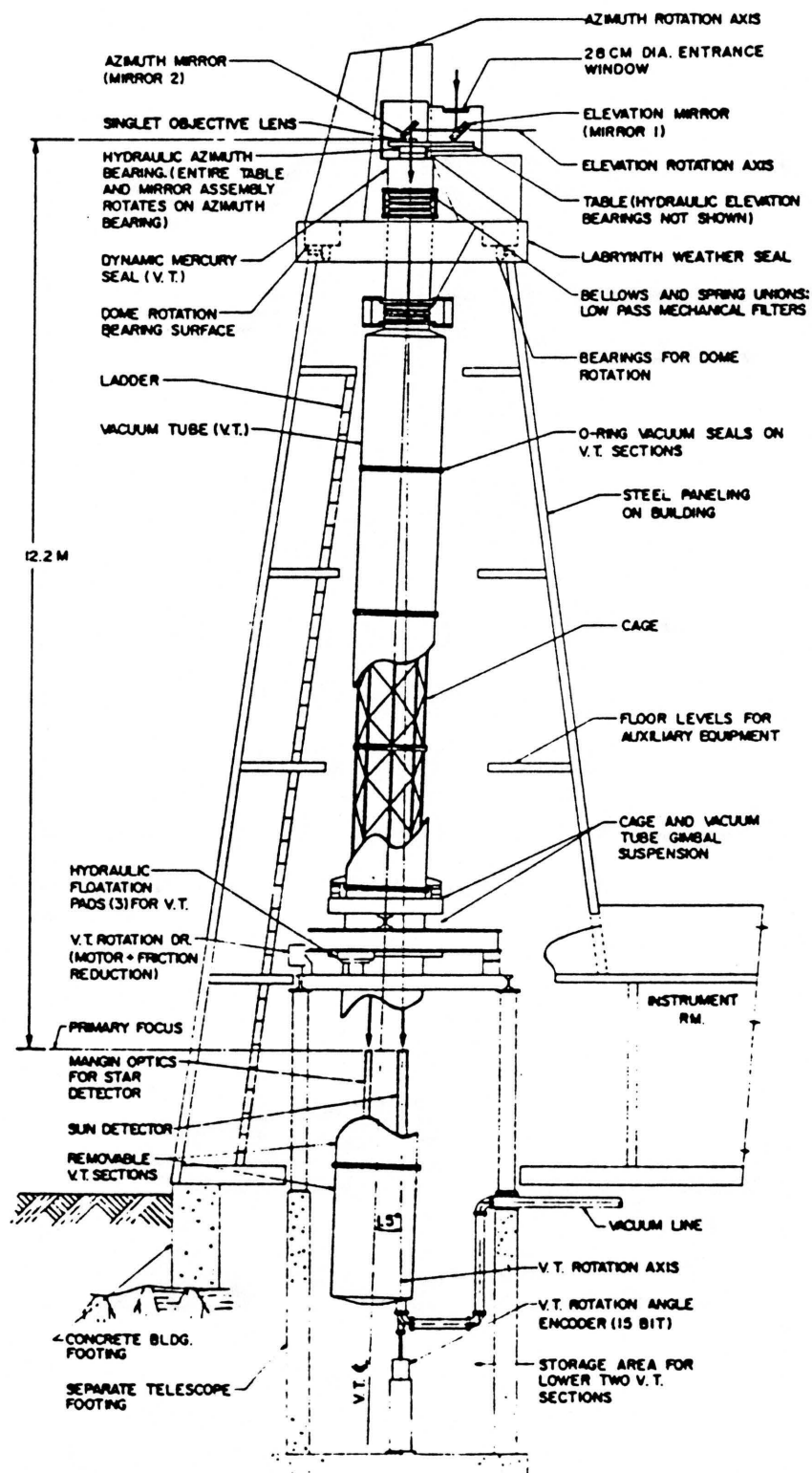


Figure 1. Cross Section of Telescope and Building.

This figure was reproduced from Stebbins (1975).

The inner cylinder rotates in elevation on a hydraulic bearing and is driven by a servo-motor through a friction drive. The table, M_1 , M_2 , and the objective all rotate (by a servo-motor) in azimuth on a hydraulic bearing located underneath the table. This bearing, along with other mechanical and flotation devices, isolates the dome optics from the building.

The objective focuses the solar image on photodetectors located at the observing platform near the bottom of the tower. The photodetectors, used for diameter measurements, and the Mangin optics, used for guiding, are attached to a support that is suspended from the table holding the dome optics by low-expansion Invar[®] tubes. Therefore, the entire optical system is free from vibration introduced from the dome or control room electronics.

Guiding is performed by a three-tiered hierarchy of servo loops. The inner loop consists of the four, folded, color correcting, Mangin systems and the M_2 mirror. Each one of the Mangin systems is located in a tube 1.25 inches in diameter and eight feet long. They are located symmetrically about the limb of the solar image. The Mangin tubes are used to position the solar image such that diameter measurements can be made by the photodetectors which are placed between the Mangin tubes in the image plane. The location of the Mangin tubes and photodetectors on the image plane are shown in figure 2. Figure 3 shows the (color correcting) tracking optics and the solar cells used in generating the error signals for the M_2 transducers that keep the

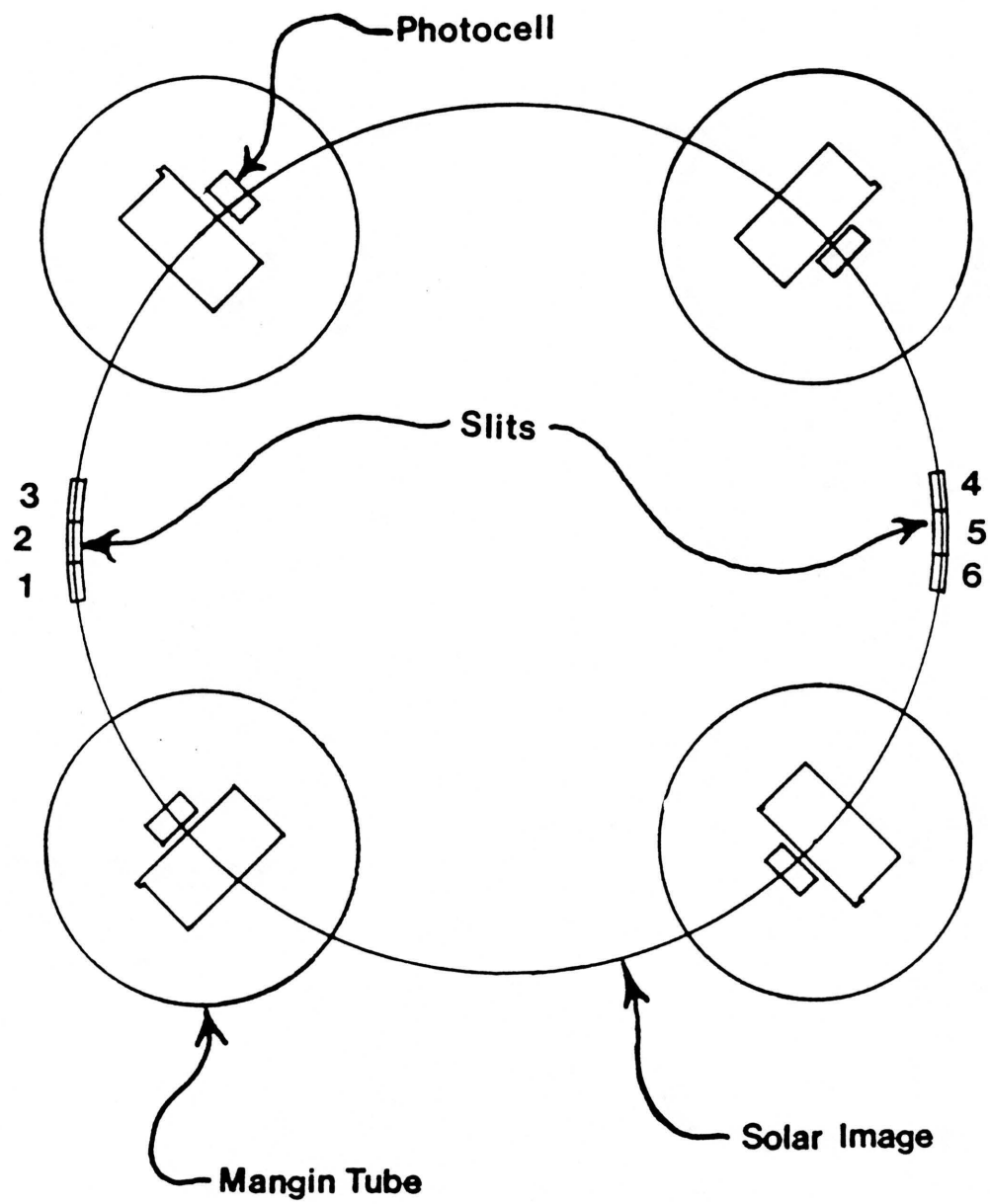


Figure 2. The Solar Image Plane.

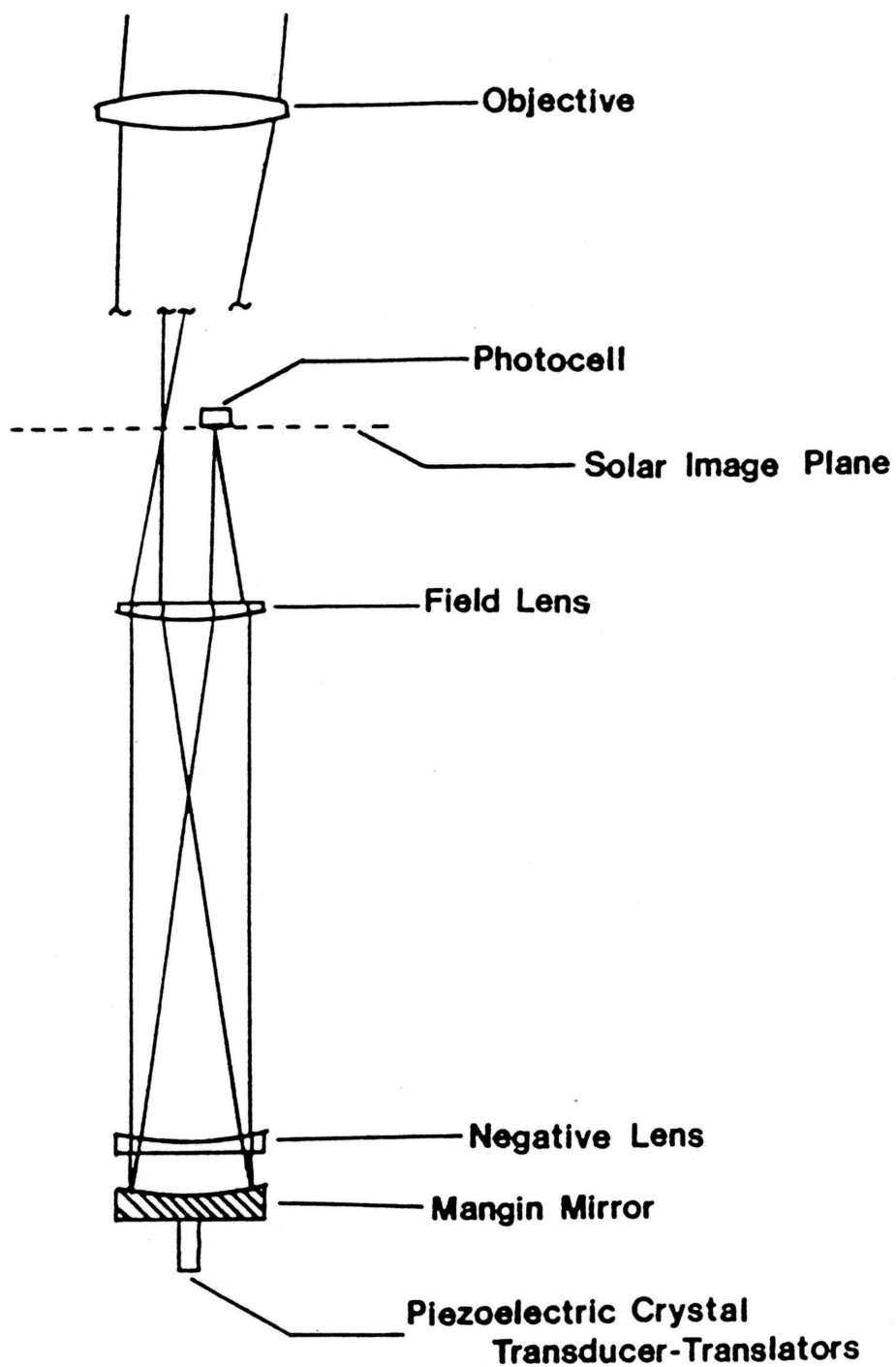


Figure 3. Mangin Tracking Optics.

image centered.

Light from the solar limb goes through the symmetrically located entrance apertures of each of the Mangin tubes at the solar image plane. The Mangin optics in each tube direct the light downward, to the bottom of the tube where a Mangin mirror is located. The light from the solar limb is next reflected back up through the remaining Mangin optics. An image of the portion of the solar limb falling on the entrance apertures is then formed on a solar cell located near the top of each tube, hence each photocell is partially illuminated by the solar limb. If the solar image starts to drift off the entrance apertures of the tubes, the illumination on the solar cells will be altered. Error signals, produced from the changing location of the limbs on the solar cells, are generated in orthogonal directions in the detector coordinate system. The two error signals from the solar cells are then transformed into the M_2 coordinate system.

The axis fixed to M_2 along the M_1M_2 direction is defined as the vertical axis, while the axis perpendicular to this direction and in the plane parallel to the solar image is defined as the horizontal axis. The error signals activate the transducers (loud speaker voice coils and magnets) located on the back of the support holding M_2 such that the solar image positioned by M_2 is moved in a direction parallel to the M_1M_2 direction (vertical axis) or perpendicular to it (horizontal axis). As the solar image is moved, the amount of the limb exposed on the solar cells is once again changed and therefore a new error signal is transformed into the M_2 coordinate system. The solar

image is positioned by the voice coils to minimize the error. The Mangin tubes are mechanically aligned such that null error signals are achieved when the solar image is in a position such that diameter measurements can be made.

The servo loop has a DC gain of the order of 1000 and an AC gain of unity at ≈ 50 Hz. The loop is designed such that the gain is proportional to $1/(\text{frequency})$ for frequencies greater than 0.1 Hz, so any global movement of the Sun with frequencies lower than about 40 Hz will be removed. This loop is the "fast servo loop" that removes rapid changes in the apparent solar position due to seeing and differential refraction changes.

Next, position transducers located on the back of M_2 create two error signals. These two signals are used to derive an error signal to move the inner cylinder holding M_1 in elevation and a second to move both the table holding M_2 and the inner cylinder holding M_1 in azimuth, such that the two position transducers located on the back of the M_2 support are servoed to null values.

Finally, the position of the dome and the outer cylinder holding the window are measured by opto-electric sensors. One sensor measures the window elevation relative to the elevation of M_1 , the other measures the azimuth of the dome relative to the azimuth of both the inner cylinder and table.

In summary, when tracking the Sun, if the solar image starts to drift off the Mangin tubes, error signals move voice coils located on the back of the M_2 support, such that the image of the Sun is

recentered on the Mangin tubes. The azimuth drive then moves both the table and the inner cylinder containing M_1 in azimuth and the elevation drive moves the inner cylinder in elevation so that position transducers on the back of the M_2 support return to their null positions. The window is then moved to align the window elevation with M_1 and the dome is moved to align the azimuth of the outer cylinder with the azimuth of the inner cylinder.

3.2 Solar Edge Definition

In the early 1970's, extensive work (see Hill, Stebbins, and Oleson 1975) was done in perfecting an edge definition of the Sun that was insensitive to seeing fluctuations, yet could still detect intensity variations in the limb darkening function. Their efforts resulted in the use of the finite Fourier transform definition (FFTD) for determining a self-consistent physical location for that place in the apparent light distribution of the Sun called its "edge".

The solar edge is said to be located at a radial distance q from the center when the following integral transform is zero:

$$F(I;q,a) = \int_{-1/2}^{1/2} I(q + a \sin \pi s) \cos 2\pi s \, ds, \quad 3.2.1$$

where I is the observed solar intensity as a function of radius and the parameter " a " is the amplitude over which the limb of the Sun is scanned.

Other edge definitions include the second derivative definition, or inflection point of the edge, as done by Böhm-Vitense (1955), and the integral definition that has been used with the Princeton oblateness telescope (Dicke and Goldenberg 1974; Dicke, Kuhn, and Libbrecht 1985, 1986). The integral definition sums intensities from two diametrically opposed apertures extending from slightly inside the edge of the Sun outward. Hill, Stebbins, and Oleson (1975) made detailed theoretical comparisons of these three techniques for the relative edge displacement in relation to a Gaussian transfer function representing atmospheric seeing. They conclude that inflection point methods are seeing sensitive and therefore not very useful as an edge location. The integral definition is far less sensitive to seeing effects and has been used successfully by the Princeton group.

However, the results of Hill, Stebbins, and Oleson (1975) show that when the aperture of the exposed limb in the integral technique is equal to the amount of limb scanned for the FFTD (6.8 arcsec), the FFTD is at least an order of magnitude less sensitive to seeing fluctuations, when the σ associated with the Gaussian transfer function is about equal to two arcseconds. This value of σ is typical of seeing conditions at the SCLERA site. Even when the atmospheric turbulence produces a very noisy and broadened apparent limb profile, Hill et al. (1975) found that the FFTD should produce less noise than the integral technique when the aperture of the exposed limb in the integral technique is comparable to the amount of the limb scanned using the FFTD. An even more important advantage of the FFTD is its high

sensitivity to changes in the solar limb-darkening function. Failure to detect such changes between the equator and pole could result in a false oblateness determination (see Hill and Beardsley 1987 and references therein).

3.3 The Detectors

There have been several major improvements in the SCLERA program since the last oblateness effort was undertaken. One of the most important improvements was the addition of more slits to sample the solar limb.

There are now two sets of slit blocks located on diametrically opposite sides of the solar image as shown on figure 2. Both blocks consist of three slits, each slit is located tangent to the limb of the Sun and they are separated from each other by about 8.3 degrees, as measured from the center of the solar image. Photodiodes are located beneath each slit; between the slits and the detectors are placed filters with bandpasses which are 8.0 nm wide (full width at half-transmission) centered at 550 nm. The scan amplitude, a , is produced by introducing a sinusoidal voltage, controlled by a microcomputer, into piezoelectric crystals located at the bottom of each of the four Mangin mirrors as shown for one of the Mangin systems in figure 3. As the mirrors are moved in phase by the sinusoidal voltage applied to the crystals, the limb of the Sun is translated across the solar cells located near the top of the Mangin tubes. The direction of the scan

introduced by the crystals is along the direction of the two diametrically opposed slit blocks. Two orthogonal error signals are then produced from the solar cells. These sinusoidal signals are transformed into the M_2 coordinate system. The transducers on the back of M_2 then produces a sinusoidal scan of the solar image across the slits. The phase of the signal arriving at the Mangin solar cells from the movement of the solar image across the Mangin tubes is 180° out of phase from the scan direction introduced by the crystals. This phase difference nearly cancels the movement of the solar limb on the solar cells created by the applied voltage on the crystals. As a result, a closed servo-loop is formed. Because of the high gain of the loop at the 1.6 Hz scanning frequency, the amplitude of the solar movement across the slits very nearly matches the amplitude of the scan introduced by the piezoelectric crystals. This feature will be analyzed in more detail in chapter 5. The amplitude of the voltage applied to the crystals has been adjusted such that an operational scan amplitude across the slits of approximately 21.5 arcsec has been achieved.

The optically filtered signals received on the photodetectors beneath the slits are amplified and electronically filtered. The DEC LSI 11/23[©] microcomputer then calculates the FFTD edge position for one of the slits in block A and one in block B. The computer controlled stepper motors then independently drive both slit blocks to their FFTD null locations on the limb of the Sun. A Michelson interferometer is used to measure changes in the relative diameter between the slit

blocks, while a white light interferometer is used to produce a fiducial so that diameter variations can be measured on a day-to-day basis.

The detector blocks can be rotated to any desired diameter of the solar image by preselecting the angle at the computer. The computer then calculates the corresponding value of the 14 bit optical encoder which is attached to the base of the rotation axis of the detectors. Servo motors rotate the detector about the axis until the encoder, which the computer monitors, is at the correct value.

3.4 The Computer

The Digital Equipment Corporation LSI 11/23[©] computer has replaced the prototype machine designed by SCLERA for oblateness and oscillation work in the 1970's. It provides the same functions as the prototype machine (Stebbins 1975), however, it has the advantage of much faster execution time and far larger memory capabilities. The addition of two 30 megabyte hard discs and disc drives have greatly increased the data acquisition capabilities. The six limb signals sent to the computer are digitized by a 12 bit A/D converter and stored on the discs. The white light and Michelson interferometer measurements, various temperature and pressure measurements, start-of-day parameters, and numerous other diagnostic information are also stored. At the end of the day, all information is transferred to magnetic tape. Since the limb profiles can be reconstructed from this information, smaller scan amplitudes than those created by the servo

system can be produced with the SCLERA Celerity computer located in the Physics Department at The University of Arizona. Later in Chapters 6, 7, and 8 it will be shown how the added spatial information obtained by calculating the diameters using several different scan amplitudes aides in the identification and removal of false oblateness signals.

This has been a substantial technological improvement over what was available in the mid-1970's. The existing computer in the 1970's calculated the FFTD edge location during data acquisition for each of the diametrically located slits (one on each side of the solar image) and then servoed the slits with stepper motors to their FFTD null positions. The relative separation between the slits was then measured using the interferometer and the results recorded. The integration time at each polar angle (defined by the angle between the north solar pole and location of one of the slits as measured from the center of the solar image) was 128 seconds with an additional 64 seconds between each polar angle to allow for the stepper motors to servo to the new edge position. Diameters at two scan amplitudes (6.8 and 27.2 arcseconds) were recorded separately for both the equator and the pole. It took approximately 13 minutes to record one differential diameter measurement at the two scan amplitudes.

With the current equipment, diameter measurements from only the largest scan amplitude in the observing program need be recorded since smaller scan amplitudes can now be formed off-line. The slit blocks are servoed to new polar angle locations every 64 seconds. There are eight logical tape records for each diameter measurement at a given

polar angle. A logical record consists of eight averaged scans from each of the six slits. Each individual scan is first digitized by the A/D's so that there are 256 intensity elements for each scan or 128 intensity elements for each limb profile. The interferometer reading, angles, and other diagnostic information are also saved on every record. The central slit in one of the slit blocks is servoed to polar angles of $\theta = 0^\circ$ (the polar diameter), $\theta = 90^\circ$ (the equatorial diameter), and $\theta = \pm 45^\circ$ (the diagonal diameters). The diameters defined by the outer slits in the slit blocks are located at polar angles of $\theta_s = 8.3^\circ$ clockwise or counter-clockwise with respect to the diameters defined by the central slits. Three sets of diameters corresponding to the six slits are found for each of the four locations around the solar image of the slit blocks. The total amount of time for an observing sequence including these four locations was ≈ 4.5 minutes.

CHAPTER 4

GENERAL SOLUTION FOR DIFFERENTIAL DIAMETER MEASUREMENTS

There are several classes of systematic error that must be understood before a reliable oblateness estimate can be made. The major categories of systematic error for oblateness measurements taken at SCLERA are listed below.

1. Scan amplitude calibration error
2. Detector misalignment
3. Terrestrial atmospheric phenomena
4. Errors fixed with respect to the M_1 coordinate system
5. Errors fixed with respect to the M_2 coordinate system
6. Limb darkening function uncertainties

The first category, the scan amplitude calibration error, is the error introduced into oblateness measurements because of the uncertainties in the amplitude of the scan introduced into the M_2 servo loop.

The second category contains an assortment of systematic errors that result from misalignment of the detector slits on the solar image plane. The sources of this error category are all fixed with respect to the observer's frame of reference. The phase between the minor axis introduced by these sources of image distortion (oblateness) and the north direction in the observer's coordinate system is ϕ_d . In this coordinate system all measurements are made relative to true north and are measured positive in the counter-clockwise direction looking down on the solar image. Because of the elevation-azimuth design of the

telescope, the North Solar Pole (NSP) will rotate as $(\eta-P-AZ-Z)$ relative to this coordinate system. Figure 4 is a diagram of the Celestial Sphere with all relevant angles labeled. On this figure, P is the position angle of the NSP and is measured positive in a counterclockwise direction from the imaginary line connecting the center of the Sun with the North Celestial Pole (NCP). η , the parallactic angle, is defined as the angle measured between the imaginary line connecting the center of the Sun with the NCP and the imaginary line drawn between the solar center and the zenith point on the Celestial Sphere. With this definition, η is negative in the morning and positive in the afternoon. AZ represents the azimuth angle of the Sun and is measured clockwise around the astronomical horizon from the true north direction on the Earth's surface. Z represents the zenith angle and is measured positive from the zenith direction.

The third category, atmospheric phenomena, represents one of the largest sources of systematic error in all previous oblateness studies. This category is primarily dominated by differential refraction (DR), with anisotropic distributions of image motion due to seeing representing a much smaller contribution. The minor axis of DR rotates as $[-(AZ+Z)]$ relative to the observer looking down on the solar image.

The next category of systematic error represents a shape introduced into the solar image that remains fixed with respect to the M_1 coordinate system. This image distortion results from a dishing (a non-infinite radius of curvature) of the elevation mirror or a

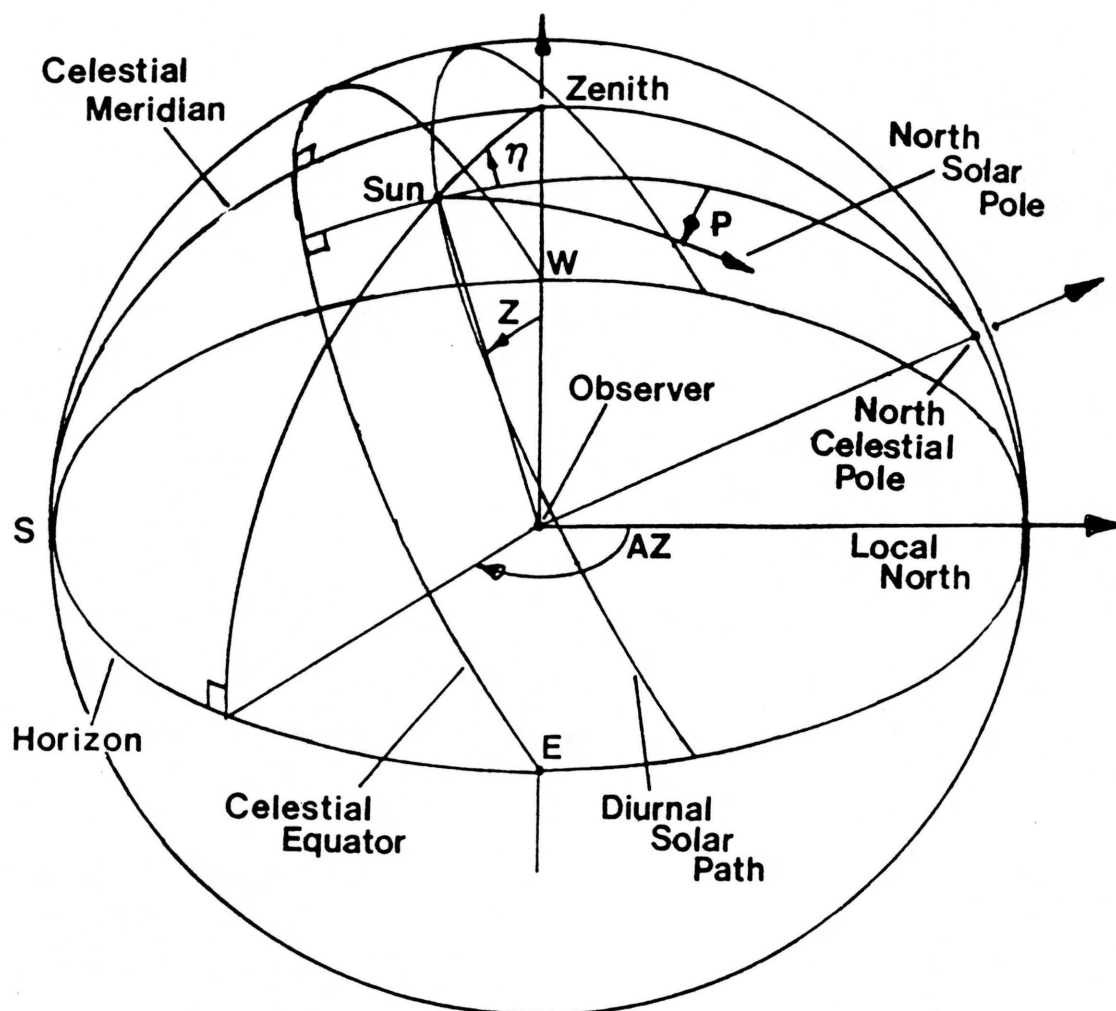


Figure 4. Celestial Coordinate System.

As described in the text, this coordinate system is used to determine the projection of the solar pole onto the image plane.

distortion in the entrance window. Both of the above contributions rotate as $[-(AZ+Z-\phi_1)]$ with respect to an observer looking down on the solar image. ϕ_1 is the phase of the distortion introduced by the mirror and window.

The fifth category of systematic error represents a shape distortion introduced into the solar image that remains fixed with respect to the M_2 coordinate system. This image distortion rotates as $[-(AZ-\phi_2)]$ relative to the observer looking down on the solar image. ϕ_2 is the constant phase associated with the distortion. This category includes dishing of the azimuth mirror (M_2) and aberrations in the objective lens. It also includes an apparent oblateness caused by mismatched electronic gains in the "fast servo loop" in the M_2 coordinate system. (If the closed loop transfer functions for the respective voice coil servo loops along the horizontal and vertical axes are not the same, a difference in scan amplitude will be produced between these two orthogonal directions. This scan amplitude difference will produce a scaling difference for the FFTD edge definition creating a false oblateness. Chapter 5 shows that this distortion is negligible.)

Differences in the solar limb darkening function between the equator and pole represent the final category of systematic error and will be discussed in chapters 6, 7, 8, and 9.

4.1 Legendre Polynomial Description of the Solar Image

Most of the systematic oblateness signals, that are introduced by the telescope, can be expressed very effectively in terms of Legendre series (see Chapter 5). In this description, an angular diameter measurement, $D(-\theta)$, of the solar image, in the solar coordinate system as observed projected down onto the solar detectors, can be written as:

$$D(-\theta) = \sum_{m=0}^{\infty} [J_m^* P_m[\cos(-\theta)] + B_m P_m[\cos(\eta-P-\theta)] + C_m P_m[\cos(\eta-P-\theta-\phi_1)] + D_m P_m[\cos(\eta-P-Z-\theta-\phi_2)] + E_m P_m[\cos(\eta-P-Z-AZ-\theta-\phi_d)]] \quad 4.1.1$$

where B_m , C_m , D_m , and E_m represent amplitudes associated with the instrumental and atmospheric distortions. These coefficients represent distortions fixed relative to the coordinate systems that are associated with differential refraction, M_1 , M_2 and detector alignment sources respectively. As defined previously, θ is the solar polar angle of the central slit in one of the slit blocks. The other slit block is located diametrically opposite the first. P_m is the Legendre polynomial of degree m and the J_m^* represent intrinsic solar structure. J_m^* is related to the J_m used in describing the gravitational potential field in chapter 2 by

$$J_m + J'_m = -J_m^* / \bar{\theta} \quad , \quad 4.1.2$$

where $\bar{\theta}$ is the mean angular diameter of the Sun.

Notice that all of the instrumental and atmospheric coordinate systems rotate with respect to the solar coordinate system. This design feature of the telescope allows the coefficients to be calculated by a least squares analysis.

Evaluating terms up to P_4 in equation 4.1.1, the following two equations can be derived:

$$\begin{aligned} \tilde{D} = \frac{35}{16} [J_4^* + B_4 \cos 4(\eta-P) + C_4 \cos 4(\eta-P+\phi_1) \\ + D_4 \cos 4(\eta-P-Z+\phi_2) + E_4 \cos 4(\eta-P-Z-AZ+\phi_d)] \end{aligned} \quad 4.1.3$$

and,

$$\begin{aligned} \Delta D \sin 2(\eta-p) + \Delta D_{45} \cos 2(\eta-P) = -\left(\frac{3}{2} J_2^* + \frac{5}{8} J_4^*\right) \sin 2(\eta-P) \\ + \left(\frac{3}{2} C_2 + \frac{5}{8} C_4\right) \sin 2\phi_1 + \left(\frac{3}{2} D_2 + \frac{5}{8} D_4\right) \sin 2(-Z+\phi_2) \\ + \left(\frac{3}{2} E_2 + \frac{5}{8} E_4\right) \sin 2(-Z-AZ+\phi_d) \end{aligned} \quad 4.1.4$$

where $\tilde{D} = [D(0)+D(-90)-D(45)-D(-45)]$, $\Delta D = [D(-90)-D(0)]$, and

$$\Delta D_{45} = [D(45)-D(-45)].$$

Equations 4.1.3 and 4.1.4 have utilized diameter measurements such that each slit block has been located at four different polar angles. There are several reasons why these angles are used. First, most sunspots occur at solar latitudes between about 5 and 35 degrees, therefore, the data obtained from these four polar angles are relatively uncontaminated by the presence of sunspots.

Next, equation 4.1.3 shows that J_4^* can be calculated without any knowledge of the relatively large amplitude P_2 terms (see amplitudes associated with P_4 and P_2 terms in tables 2 and 3

respectively) associated with the telescope. Estimates of J_4^* have not been presented in previous solar oblateness studies.

Equation 4.1.4 also shows that the M_1 term is a constant and therefore can be completely removed by subtracting dc components from both sides of the equation. Even more importantly, the P_2 atmospheric coefficient has been removed from both equations. This coefficient depends on zenith angle and the local atmospheric refraction law. ΔD_{45} effectively measures the local differential refraction in equation 4.1.4, making the removal of B_2 possible without reference to any theoretical atmospheric refraction law.

Higher order atmospheric terms can be shown to be negligible by using the third-order refraction law (Smart 1977),

$$\delta Z = (n-1+b) \tan Z + b \tan^3 Z \quad 4.1.5$$

where δZ represents the refraction correction in the zenith direction, n is the index of refraction, and b is proportional to the mass of a column of air above the telescope for an atmosphere consisting of spherical layers. For a nonspherically stratified atmosphere, b will depend on the density profile of the atmosphere. Using equation 4.1.5 and plane trigonometry, the following correction to orthogonal differential diameter measurements can be made:

$$\Delta D_Z = \bar{\theta} [(n-1) + 3b \sec^2 Z] \tan^2 Z \cos 2(\pi - P - \theta_p) , \quad 4.1.6$$

where $\Delta D_Z = [D(90+\theta_p) - D(\theta_p)]_Z$ is the correction for differential refraction, and θ_p is the polar angle to which the correction is applied. Equation 4.1.6 can be compared with results from spherical trigonometry using the same refraction law. For $Z \leq 70^\circ$ (i.e. for solar altitudes $> 20^\circ$), there is less than 1 milliarcsecond difference between the two methods for any reasonable value of n and b . This shows that equation 4.1.6 is a very good approximation for any local values of n and b . By comparing equation 4.1.6 with ΔD found from equation 4.1.1

$$-\frac{3}{2} B_2 = \bar{\theta} [(n-1) + 3b \sec^2 Z] \tan^2 Z . \quad 4.1.6$$

The B_2 coefficients have been removed from equations 4.1.3 and 4.1.4, and since the B_2 coefficient very accurately represents differential refraction for $Z < 70$ degrees, higher order differential refraction terms in equations 4.1.3 and 4.1.4 should be extremely small. The only known exception to this result is if the local topography around the telescope introduces a refraction gradient with a horizontal component. This situation may have arisen for oblateness work done by the Princeton group at Mt. Wilson (Libbrecht 1984, Dicke, Kuhn, and Libbrecht 1985, 1986). However, the SCLERA site has been chosen to minimize the effects of local topography. The telescope is located in the Santa Catalina Mountains on a relatively flat (except for a few hills to the south) plateau. The prevailing winds come up from the valley floor over a ridge several miles away from the

telescope site creating a smooth laminar flow by the time the wind reaches the site. Therefore the type of anisotropy encountered at Mt. Wilson is not expected. In Section 7.3, the possible magnitude of this effect is investigated.

4.2 General Solution for J_2^* and J_4^*

The observed values of $D(-\theta)$ can be solved for J_4^* and J_2^* directly by conventional least squares techniques. However, because of the nature of the frequency spectrum of the noise, a more efficient analysis can be achieved with a "prefiltering" of the $D(-\theta)$. The noise is introduced by a combination of changing detector alignment (see chapter 5), oscillating atmospheric differential refraction over the timescale of one complete set of diameter measurements (4 1/2 minutes for all four polar angles), and solar oscillations. The prefiltering process can be described as a phase-sensitive detection technique.

The general approach is to apply a Fourier transformation on each term of the right hand side of equations 4.1.3 or 4.1.4 using the same window function over which the diameter measurements are taken. The mean time of each set of four polar angles is used to calculate Z , AZ , and η . The sine or cosine of the various combinations of angles found in the two equations are then calculated. This process is executed for every set of diameter measurements. Each term is then Fourier transformed to create a theoretical spectrum representing the cosine or sine component of each source of systematic oblateness.

Next, the left hand side that includes the observations are Fourier transformed. The equations are then arranged to be in the form

$$\sum_{j=0}^{N-1} G(j\Delta\nu) F_1^*(j\Delta\nu) = \sum_{k=1}^M A_k \left(\sum_{j=0}^{N-1} F_k(j\Delta\nu) F_1^*(j\Delta\nu) \right),$$

$$\sum_{j=0}^{N-1} G(j\Delta\nu) F_2^*(j\Delta\nu) = \sum_{k=1}^M A_k \left(\sum_{j=0}^{N-1} F_k(j\Delta\nu) F_2^*(j\Delta\nu) \right), \quad 4.1.8$$

"

"

"

"

$$\sum_{j=0}^{N-1} G(j\Delta\nu) F_M^*(j\Delta\nu) = \sum_{k=1}^M A_k \left(\sum_{j=0}^{N-1} F_k(j\Delta\nu) F_M^*(j\Delta\nu) \right),$$

where $\Delta\nu$ is the sampling frequency interval of the Fourier transforms, N represents the number of frequencies summed over, G is the Fourier transform of the left hand side of equation 4.1.3 or 4.1.4, M is the number of theoretical transform terms (F_k) in each equation, and F_k^* represents the complex conjugate of F_k . The F_k are the following:

Eq. 4.1.3

$$\begin{aligned}
F_1 &= FT[1] \\
F_2 &= FT[\cos 4(\eta-P)] \\
F_3 &= FT[\sin 4(\eta-P)] \\
F_4 &= FT[\cos 4(\eta-P-Z)] \\
F_5 &= FT[\sin 4(\eta-P-Z)] \\
F_6 &= FT[\cos 4(\eta-P-Z-AZ)] \\
F_7 &= FT[\sin 4(\eta-P-Z-AZ)]
\end{aligned}$$

Eq. 4.1.4

$$\begin{aligned}
&FT[\sin 2(\eta-P)] \\
&FT[\cos 2(-Z)] \\
&FT[\sin 2(-Z)] \quad 4.1.9 \\
&FT[\cos 2(-Z-AZ)] \\
&FT[\sin 2(-Z-AZ)]
\end{aligned}$$

where FT represents the Fourier transform of the quantity in brackets.

In this notation the A_k represent:

Eq. 4.1.3

$$\begin{aligned}
A_1 &= \frac{35}{16} J_4^* \\
A_2 &= \frac{35}{16} C_4 \cos 4(\phi_1) \\
A_3 &= -\frac{35}{16} C_4 \sin 4(\phi_1) \\
A_4 &= \frac{35}{16} D_4 \cos 4(\phi_2) \\
A_5 &= -\frac{35}{16} D_4 \sin 4(\phi_2) \\
A_6 &= \frac{35}{16} E_4 \cos 4(\phi_d) \\
A_7 &= -\frac{35}{16} E_4 \sin 4(\phi_d) .
\end{aligned}$$

Eq. 4.1.4

$$\begin{aligned}
&-(\frac{3}{2} J_2^* + \frac{5}{8} J_4^*) \\
&(\frac{3}{2} D_2 + \frac{5}{8} D_4) \sin 2(\phi_2) \\
&-(\frac{3}{2} D_2 + \frac{5}{8} D_4) \cos 2(\phi_2) \quad 4.1.10 \\
&(\frac{3}{2} E_2 + \frac{5}{8} E_4) \sin 2(\phi_d) \\
&-(\frac{3}{2} E_2 + \frac{5}{8} E_4) \cos 2(\phi_d)
\end{aligned}$$

Notice that B_4 atmospheric terms have been excluded because of their projected small amplitudes. Also for equation 4.1.4, the mean

values for the entire data set have been subtracted from both sides of the equation before the Fourier transforms are calculated. This removes the amplitudes associated with M_1 -type errors in equations 4.1.8, 4.1.9, and 4.1.10.

Equations found in 4.1.8 can now be solved by using least squares techniques for the A_k that represent either equation 4.1.3 or 4.1.4. There are several advantages of this technique over the direct least squares approach. First, there are only $2M$ (M real plus M imaginary) equations each with M coefficients. A least squares solution of equation 4.1.3 or 4.1.4 would involve over 1000 normal equations, one for each set of diameter measurements. A second advantage is the ability to filter high frequency noise so that only low frequency systematic error harmonics remain. The filtering is achieved by modifying N in the equations represented by 4.1.8 to include only the desired frequency range. This can reduce noise without introducing systematic errors because instrumental terms have almost all of their harmonics located at the lower frequencies in the spectrum. A final advantage of this method is the ability to choose portions of the low frequency spectrum to sum. If these regions are chosen such that only the largest amplitude peaks in the theoretical spectrum are used, then this phase sensitive detection could greatly improve signal-to-noise and, therefore, the accuracy to which the A_k can be determined.

CHAPTER 5

SYSTEMATIC ERRORS INTRODUCED BY THE TELESCOPE

In Chapter 4 was described the representation of the solar image in terms of Legendre series expansions. This chapter will investigate this description for the various sources of systematic oblateness introduced by the telescope.

5.1 Optical Sources of Image Distortion

Almost all image aberrations introduced by the optics create an ellipsoidal image distortion. This includes dishing of the elevation and azimuth mirrors, and astigmatism introduced by the entrance window and objective.

In the previous oblateness study at SCLERA (Hill and Stebbins 1975), the maximum $\Delta D/D$ introduced by any of the above sources was about 1×10^{-4} . The P_2 and P_4 terms of a Legendre series should accurately represent an elliptical distortion of this small magnitude. In chapter 7 it will be shown that the amplitudes of the P_4 coefficients are about an order of magnitude smaller (≈ 10 milliarcseconds) than that found for the P_2 terms. Because of the small value of the P_4 coefficients, higher order Legendre coefficients describing the distortion should be unimportant.

There are two sources of optical aberration that may not be well described by the first few terms of a Legendre series with

constant coefficients. First, morning thermal gradients created by solar heating of the elevation and azimuth mirrors can introduce time varying components of C_m and D_m found in equation 4.1.1. Hill and Stebbins (1975) used available information about the rate at which the mirrors heated in the morning to estimate an error of $\sigma_{th} < 0.2$ milliarcseconds in their differential diameter measurement. At that time the mirrors were made of fused silica. The current optical design used low expansion Cer-Vit[®] material for the mirrors which reduced the thermal expansion by a factor of five. Therefore σ_{th} should be negligible for current oblateness work.

The other optical source of image distortion was the existence of a wedge formed in the glass of the entrance window (non-parallel surfaces) that created a secondary image displaced 45 ± 15 arcseconds from the primary. The wedge was designed into the system when the telescope was used for deflection of starlight experiments in the 1960's and 1970's. The wedge aided in the determination of the stellar centroid by removing nearby secondary images.

The wedge introduces a more complicated distortion in the image plane than a simple ellipse. The intensity of the secondary image is 1.8×10^{-3} times the primary and the amplitude of the spurious oblateness is dependent on the scan amplitude used in the FFTD edge definition.

Hill and Stebbins (1975) found that the amplitude associated with this distortion was irregular and varied between 0.4 and 1.6 milliarcseconds, however, the contribution to the error (σ_w) in their

differential diameter measurement was less than 0.3 milliaroseconds. The errors of the current work should be lower because of the added advantage of fitting this distortion with P_4 as well as the $\cos 2(\pi P + \phi_1)$ term that Hill and Stebbins used.

5.2 Distortions Introduced by the Servo Loop

The servo loop introduces an apparent oblateness that rotates as an M_2 type distortion in the image plane. As stated previously, this is caused from mismatched transfer functions between the horizontal and vertical axis transducers of M_2 . This mismatch occurs in the open loop gain of the system. For the closed loop system,

$$a_\xi = \frac{a_0}{1 + \frac{1}{G_\xi}}, \quad 5.2.1$$

where $G_\xi(t)$ represents the open loop gain of the system at the scanning frequency, a_0 represents the amplitude for an infinite gain system, and a_ξ is the amplitude of the scan across the slits and Mangin tubes. ξ is the angle of the scan relative to the M_2 coordinate system.

Using this relationship and an analytic expression for the FFTD edge definition, Hill and Stebbins (1975) derived an expression relating the gain difference along the two orthogonal axes in the M_2 coordinate system to an error amplitude associated with the FFTD edge definition. This equation can be modified such that:

$$\approx \frac{3}{2} c_2(a_i, t) \approx 0.102 \frac{\Delta G}{G^2} \frac{a_i^{3/2}}{(1 + 1.083 a_i^{1/2})}, \quad 5.2.2$$

where $c_2(a_i, t)$ is the time varying component associated with C_2 in equation 4.1.1 such that $C_2 = C + c_2(a_i, t)$, C is a constant, ΔG represents the difference in gain along the two orthogonal axes of the M_2 coordinate system and a_i is equal to the scan amplitude (in arcsec) used to calculate the lock-on points from the recorded limb profiles.

For the 1983 data set $\Delta G/G < 0.05$ and $15 < G < 20$. Using $\Delta G/G = 0.05$, $a_i = 21.5$ and $G = 15$, an upper limit for $c_2(a_i, t)$ can be found to be less than 5 milliarcseconds from equation 5.2.2. Since M_2 -type errors rotate over a range of 172° with respect to the solar pole during the observing season, systematic contribution from this source to J_m^* is removed in the data reduction.

Hill and Stebbins found that $c_2(a_i, t)$ contributed an error of $\sigma_{sv} < .03$ milliarcseconds to their mean value of ΔD . Since $\Delta G/G < .1$ for their work and π -P-Z changed over a much smaller range than for the current work, σ_{sv} should be extremely small. Therefore this term will be neglected in the analysis discussed in chapter 7.

More evidence supporting the assumption that C_m and D_m are constant are the errors associated with these coefficients. Tables 2 and 3 show that these errors are only a few milliarcseconds. If these terms are significantly time varying, the errors would be much larger. Also, within the uncertainties placed on the C_m and D_m , there is not any systematic trend as a function of scan amplitude. This suggests

that wedge effects from the window, and the apparent oblateness caused from the servo loop are small.

5.3 Scan Amplitude Calibration

Assigning an incorrect scan amplitude to the recorded limb profiles will introduce a scaling error (σ_s) into differential diameter measurements such that $\sigma_s = (\sigma_a/a) \Delta D$, where σ_a is the scan amplitude error.

The scan amplitude was calibrated by, first, orienting the position angle of the slit blocks to point along the same direction as the horizontal axis of the M_2 coordinate system. Next, a series of limb scans were recorded with the slits servoing at their equilibrium FFTD null edge positions. The stepper motor controlling the slit locations for one of the slit blocks (side B) was then turned off. This allowed a two arcsecond mechanical repositioning of this slit block toward the image center. Another set of limb scans was recorded with one side servoing close to the FFTD null position while the other was still located inside the FFTD null position. Side B was then moved another two arcseconds toward the center of the solar image and the procedure repeated. This process was continued until side B was located about 14 arcseconds inside the FFTD null position as monitored by the interferometer. Next, the position angles of the slit blocks were relocated so that they were aligned along the vertical axis of M_2 and the entire process was repeated with sides A and B first servoing to their null positions. Both horizontal and vertical directions were

scanned twice using this procedure. The scan information was then transferred to tape and analyzed at The University of Arizona.

The lock-on points q (see equation 3.2.1), were calculated from the recorded limb profiles using a scan amplitude of $a_s = 27.2$ arcsec. An average value of the lock-on points, \bar{q} , was first calculated when both slit blocks were servoed to their null positions. The interferometer values corresponding to these lock-on points were also averaged (\bar{D}_I). Next, lock-on point differences (Δq) were calculated between \bar{q} and individual values of q found when slit block B was located inside the edge location. ΔD_I , the corresponding interferometer difference, can be compared with Δq . A linear least squares fit of $\Delta q = k \Delta D_I$ where k is the least squares coefficient, was then made for each of the four sets of measurements.

Since Δq scales linearly with the assumed scan amplitude a_s , the true scan size across the slits is $a = a_s/k$. The mean value of the four sets of measurements is $\bar{k} = 1.267 \pm 0.011$, hence, the value of $\bar{a} = 21.5 \pm 0.2$ milliarcseconds. All of the lock-on points for the 1983 data set have been calculated at assumed scan amplitudes of a_s , $3 a_s/4$, $a_s/2$, and $a_s/4$. These lock-on points are therefore divided by \bar{k} to find corrected values of q at scan amplitudes of 21.5, 16.125, 10.75, and 5.375 arcseconds respectively. Using $\sigma_a = \pm 0.2$ and $\bar{a} = 21.5$ milliarcseconds, we find $\sigma_s < \pm 0.01 \Delta D$, or scaling errors result in less than a one percent systematic error in J_2^* or J_4^* .

5.4 Detector Alignment Errors

There are three sources of distortion resulting from the detector misalignment: the first is an elliptical image distortion introduced by the rotation axis of the detector being tilted with respect to the optical axis of the telescope. The second source is also an elliptical distortion introduced by the tilt of the detector plane with respect to the rotation axis. Both of these distortions can be described well by the P_2 term in equation 4.1.1 for detector type errors.

The third type of distortion is caused by the two slit blocks in the detector plane being translated on the solar image such that chordal measurements are found instead of diameters. If the magnitude of the translation for each of the four polar angle locations of the slit blocks is the same, then an unimportant error (σ_{cd}) will result ($\sigma_{cd} < .001$ milliarcseconds for a 5 arcsecond translation). However, because of power and signal cables connected to the base of the rotation axis of the solar detectors, a small torque is applied which alters the rotation axis alignment when the axis is turned: this torque is dependent on the location of the slit blocks with respect to the observer's coordinate system. Therefore, the slit blocks (and therefore six slits) will be translated by varying amounts on the image as the detector is rotated. The apparent image shape, as measured by the detectors, resulting from this misalignment is very irregular. This distortion cannot be represented very well by the first few terms of a Legendre series: also, the coefficients change throughout the

day. Fortunately, information available from the three slits located in each slit block enables this distortion to be corrected.

Let $D_{m,n}(-\theta, a)$ represent a diameter or chord measurement between slit blocks A and B. The subscripts $m = 1, 2$, and 3 are labels for the three slits in block A while $n = 4, 5$, and 6 are labels for the three slits in block B as shown on figure 2. $D_{2,5}$ has been defined as the diameter measurement made between the central two slits. $D_{1,4}$ and $D_{3,6}$ represent the other two diameter measurements taken at $\theta_s = 8.3 \pm 0.5$ degrees clockwise or counter-clockwise with respect to the central diameter measurement. When $D_{2,5}$ is located at the equator, $D_{1,6}$ and $D_{3,4}$ represent chordal measurements either above or below the equator. If $D_{2,5}$ is located exactly on the diameter of the solar image, then $(D_{1,6} - D_{3,4}) = K$ should be nearly zero. However, because it is difficult to position the slit blocks such that all six slits are tangent to the limb of the sun, K will in general not be zero. After carefully positioning $D_{2,5}$ on a diameter by monitoring the relative diameter of the solar image with the interferometer, it is found that $K = 4.56 \pm 0.36$ arcseconds for the 1983 data set.

To a very good first-order approximation it can be shown that:

$$D_{1,6} - D_{3,4} - K \approx 4 V \tan \theta_s \quad 5.4.1$$

and,

$$\delta D_{cd}(-\theta) \approx V^2/\bar{\theta} \quad , \quad 5.4.2$$

where V is the translation of the slit blocks, on the solar image, in a direction perpendicular to the scan, and $\delta D_{cd}(-\theta)$ represents the correction necessary to convert $D_{2,5}$, $D_{1,4}$, and $D_{3,6}$ into diameter measurements. Using these two equations

$$\delta D_{cd}(-\theta) \approx (D_{1,6} - D_{3,4} - K)^2 / (16 \bar{\theta} \tan^2 \theta_s) \quad . \quad 5.4.3$$

Each value of $D_{2,5}$, $D_{1,4}$, and $D_{3,6}$ calculated from the 1983 data set is corrected by equation 5.4.3. The mean values for the differential corrections in units of milliarcseconds are:

$$\begin{aligned} \overline{\Delta d} &= \overline{\delta D_{cd}(-90) - \delta D_{cd}(0)} = -8.9 \pm 2.0 \quad , \\ \overline{\Delta d}_{45} &= \overline{\delta D_{cd}(45) - \delta D_{cd}(-45)} = 4.7 \pm 1.7 \quad , \quad 5.4.4 \\ \tilde{d} &= \overline{\delta D_{cd}(-90) + \delta D_{cd}(0) - \delta D_{cd}(45) - \delta D_{cd}(-45)} = -5.5 \pm 1.5 \quad . \end{aligned}$$

The bars over the quantities represent the average value of the correction for the entire 1983 data set. The errors represent the average one sigma error associated with each set of observed polar angles. This error results from the uncertainties in K and θ_s . Random errors that are created by changes in the limb darkening function or differential refraction do not alter the mean values so these estimates are not included in the calculation of the uncertainties.

Equation 5.4.4 shows that a systematic error would result in differential diameter measurements if these corrections are not made.

The errors represent the accuracy to which the correction can be applied to remove systematic errors in J_m^* .

CHAPTER 6

OBSERVATIONS

The 1983 oblateness observations were taken between June 19, 1983 and July 20, 1983. The data represents a time interval of 32 days. Observations began around 6:30 am and ended approximately 6:30 pm when weather conditions were acceptable. During this time interval, several thousand sets of diameter measurements were recorded.

Figure 5 shows the diameter observations for day number 180. The vertical axis is divided into four sections: starting from the top, the four segments correspond to polar angles of $\theta = -45^\circ, 45^\circ, 90^\circ$ and 0° respectively. A constant value, \bar{D} , has been subtracted from each diameter measurement to change the zero points for plotting purposes. The horizontal axis represents time measured in seconds from midnight. In each section there are three curves labeled to correspond to $D_{3,6}(-\theta, a_4)$, $D_{1,4}(-\theta, a_4)$, and $D_{2,5}(-\theta, a_4)$ where the scan amplitude $a_4 = 21.5$ arcseconds. These three sets of diameter measurements would overlap if the slits were exactly tangent to the limb of the sun and if the limb darkening functions were identical.

The diameter measurements presented on the figure have been corrected for translation onto a chord by equation 5.4.3. Brief time periods (five to ten minutes) when clouds would have been interfering with observations are also replaced by the mean value of the previous three unaffected diameter measurements. The dominant feature in this

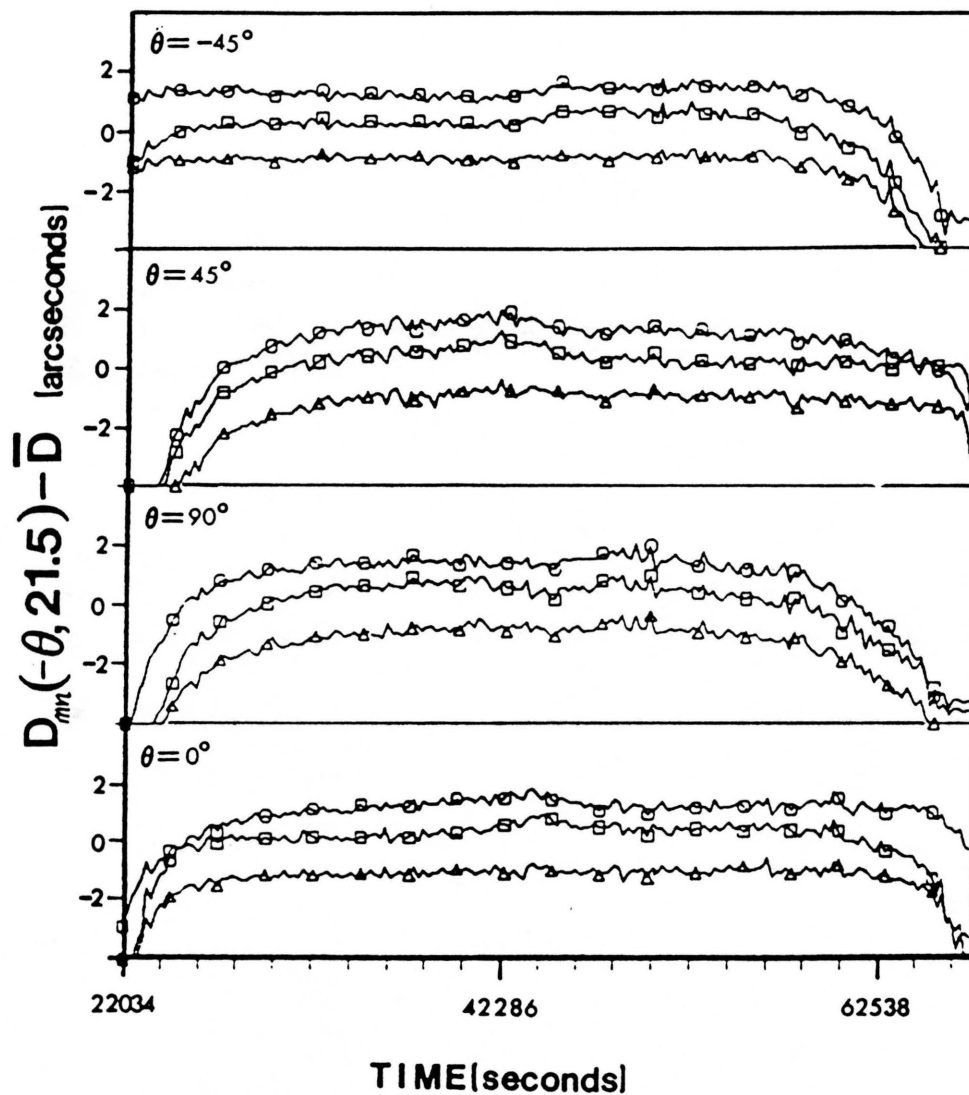


Figure 5. $D_{m,n}(-\theta, 21.5)$ Vs. Time for day number 180.

A constant value, \bar{D} , has been subtracted from all diameter measurements. The squares represent $D_{1,4}(\pm\theta, 21.5)$; the triangles represent $D_{2,5}(-\theta, 21.5)$; and the circles represent $D_{3,6}(-\theta, 21.5)$. Every 10th value has been labeled.

figure is differential refraction early in the morning and late in the afternoon.

The measurements used to find J_2^* and J_4^* had to satisfy several selection criteria. The first criterion was based on the magnitude of the chordal correction. There were two days when the mean value (for each day) of the correction was very large [$\delta(-90) \approx 34$ marcseconds] with $V > 8$ arcseconds in equation 5.4.2. The mean value of V for each of the other days was typically three arcseconds. Since the accuracy to which the correction can be applied is proportional to V , it was possible that these two days may introduce systematic error into the data and therefore they were excluded from further analysis.

The next selection criterion involved a test for appropriate atmospheric conditions. As shown in equation 4.1.3, \tilde{D} is independent of P_2 type image distortions. Therefore, since P_4 instrumental and atmospheric terms are believed to be small, changes in \tilde{D} represent clouds, changes in the solar limb darkening function for at least one of the four values of θ , or short timescale fluctuations (less than 4 1/2 minutes) in local differential refraction.

Plotting $\tilde{D}_{m,n}(a)$ and $D_{m,n}(-\theta, a)$ for the entire data set, it was possible to identify periods of time when the above processes were interfering with observations. When just a few values of \tilde{D} and D were affected by clouds, the individual diameter measurements were replaced with the mean value of the previous three unaffected diameters. The data containing extended periods of time when clouds were interfering were excluded from further analysis. A more sophisticated approach of

interpolation for the diameters altered by spurious clouds was not necessary because of the small number of diameters involved. Furthermore, the type of noise introduced into the analysis from a few sporadic clouds would be high frequency in nature and could almost be completely eliminated using the phase-sensitive detection technique described in chapter 4.

Early in the morning and in particular, in the late afternoon (thermal convection cells rise off of the desert floor in the afternoon) when $Z \geq 70^\circ$ the noise level greatly increased. Due to this noise, coupled with the possibility of P_4 and higher order, systematic, atmospheric terms affecting results, all measurements used to find J_2^* and J_4^* were made at $Z \leq 70^\circ$, with approximately 66% of this set of observations taken at $Z \leq 50^\circ$ and 87% taken at $Z \leq 60^\circ$.

Figure 6 shows $\tilde{D}_{m,n}(a_4)$ vs time for day number 180. The subscripts of \tilde{D} correspond to the slit labels defined in chapter 5 for $D_{m,n}(-\theta, a)$. \tilde{D} is measured in arcseconds and time is measured in seconds from midnight. The vertical axis is subdivided into three sections. Starting from the top they represent $\tilde{D}_{3,6}$, $\tilde{D}_{2,5}$, and $\tilde{D}_{1,4}$, respectively. Corrections for short periods of clouds and translations are made in the same way as for the previous figure.

The high frequency noise (removed using the phase-sensitive detection technique) is believed to be caused from short timescale changes in differential refraction. However, longer time scale trends that could affect J_4^* appear to be small. This indicates that most long term systematic atmospheric and instrumental errors are removed in \tilde{D} .

Another selection criterion is based on the sensitivity of the FFTD edge definition to changes in the limb darkening function. These changes can most easily be identified by comparing diameters calculated using two different scan amplitudes at the same polar angle. The diameter difference is almost unaffected by differential refraction and atmospheric seeing conditions. This property and its high sensitivity to changes in the limb darkening function make it an extremely useful parameter to study for both oblateness work and solar oscillations.

As an example, a plot of $[D_{m,n}(-\theta, a_1) - D_{m,n}(-\theta, a_4)]$ vs. time for day number 171 is shown in figure 7. $D_{m,n}(-\theta, a_1)$ corresponds to the diameter measurement made using the smallest scan amplitude (5.38 arcseconds) and $D_{m,n}(-\theta, a_4)$ is the diameter measurement corresponding to the largest scan amplitude (21.5 arcseconds). The horizontal scale, time, is measured in seconds. The four sections of the plot correspond to the diameters found at the four values of θ as shown in figure 5. Each section contains the three diameter measurements found from the six slits. $[D_{m,n}(-\theta, a_1) - D_{m,n}(-\theta, a_4)]$ plotted on the figure had a mean value of 4.44 arcseconds subtracted from each measurement.

If the limb darkening function does not change around the 360° circumference of the solar image, then all values of $[D_{m,n}(-\theta, a_1) - D_{m,n}(-\theta, a_4)]$ would coincide for the four values of θ and three different combinations of indices (m,n) that label diameters. Inspection of the figure clearly shows this not to be the case, especially for the equatorial diameters. Comparing the Boulder sunspot diagrams (from Solar-Geophysical Data prompt reports, July

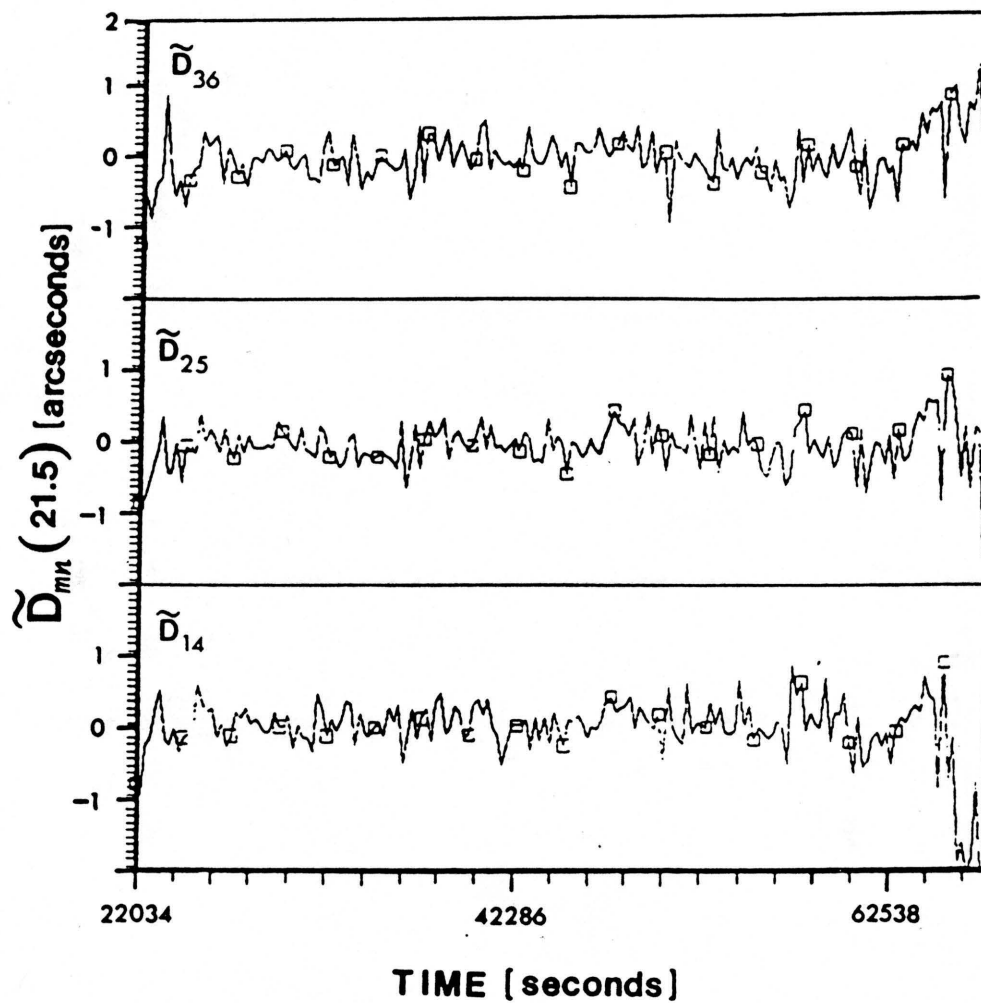


Figure 6. $\tilde{D}_{m,n}(21.5)$ Vs. Time for day number 180.

Every 10th value has been labeled with a square.

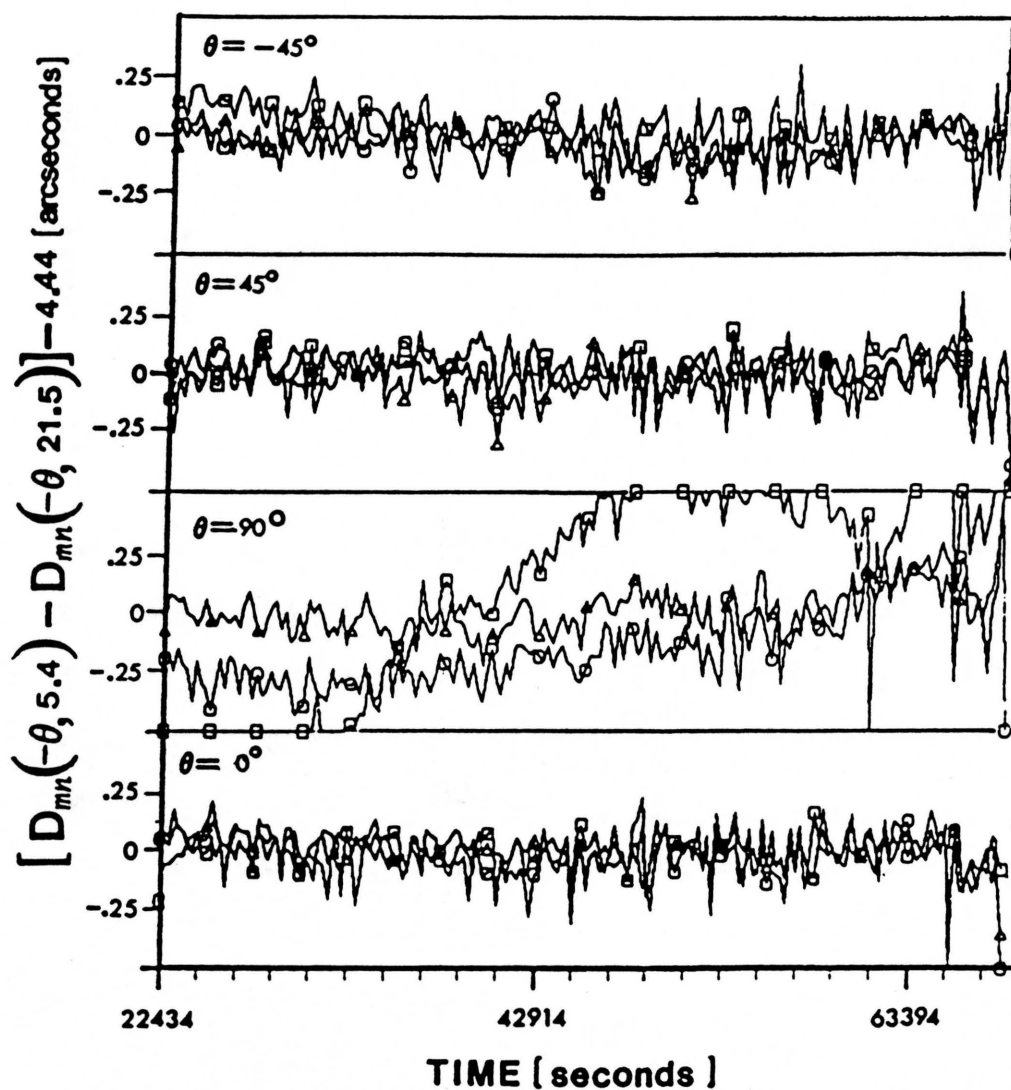


Figure 7. $D_{m,n}(-\theta, a_1) - D_{m,n}(-\theta, a_4)$ vs. Time for Day Number 171.

The difference in solar diameters at a given polar angle using two different scan amplitudes. The squares on the figure represent $[D_{1,4}(-\theta, 5.4) - D_{1,4}(-\theta, 21.5)]$; the triangles represent $[D_{2,5}(-\theta, 5.4) - D_{2,5}(-\theta, 21.5)]$; and the circles represent $[D_{3,6}(-\theta, 5.4) - D_{3,6}(-\theta, 21.5)]$. Every 10th value has been labeled.

1983) with this data, it is apparent that a small sunspot moved within 5 degrees of slit 1. The surrounding active region must have been responsible for the large variations for $[D_{1,4}(-\theta, a_1) - D_{1,4}(-\theta, a_4)]$. On other days, large variations are frequently observed using this type of differential measurement without sunspots or obvious active regions located near the limb. This is expected because of the ability of the FFTD to detect small changes in the limb darkening function that are unobservable using other techniques.

After examining each day using several different combinations of $[D_{m,n}(-\theta, a_i) - D_{m,n}(-\theta, a_j)]$, the data set was reduced to include only those diameter measurements which were relatively free from apparent differences in the limb darkening function between the four polar angles. $|D_{m,n}(-\theta, a_i) - D_{m,n}(-\theta, a_j)|$ had to depart from its mean value for a given day less than, approximately, 0.25 arcseconds for each of the four polar angles before the set of diameters was included in the least squares analysis. The values of (i,j) normally used in the selection criteria were $(1,4)$, $(2,4)$, and $(3,4)$. However, sometimes other combinations of (i,j) were used in conjunction with the previous three. If the selection criteria were not met for a particular combination of (i,j) , then diameters at all polar angles corresponding to this time were rejected for the indices (m,n) . Three separate data sets were generated for the three combinations of (m,n) .

It was apparent that most of the changes in the limb darkening function were occurring near the equator and not the pole or polar angles of ± 45 degrees. Furthermore, the diameter measurements

corresponding to $D_{1,4}$ and $D_{3,6}$ taken near (± 8.3 degrees) the equator were far noisier than $D_{2,5}$ taken at the equator. This was expected because of the encroachment of the outer slits into the sunspot belt of the Sun's lower latitudes. Examination of the plots revealed that $D_{2,5}$ was relatively free of these active regions.

The preceding procedure removes active regions or other large diameter changes due to differences in the limb darkening function. However, small diameter differences introduced by solar oscillations or long timescale changes in the limb darkening function are still a possible source of false oblateness. The following section introduces a method to remove these sources of systematic error from J_4^* and J_2^* .

6.1 Systematic Errors Introduced by Changes in the Limb Darkening Function

Hill and Stebbins (1975) introduced an excess brightness parameter into their oblateness work defined by

$$E = \Delta D(a_2^*) - \Delta D(a_1^*) \quad 6.1.1$$

where $a_2^* = 27.2$ arcseconds and $a_1^* = 6.8$ arcseconds. Models derived from Ingersoll and Spiegel (1971) and Chapman and Ingersoll (1972) were used to find a correction (to differential diameter measurements) of $\Delta d_e = 0.93 E$. This was consistent with the findings of Hill and Stebbins concerning the observed ratio of Δd_e to E ($\Delta d_e/E = 0.46 \pm 0.25$, from Stebbins 1975). Although Hill and Stebbins used days such that the mean value of E for those days was small, the error associated with

Δd_e was still the dominant source of error for their oblateness measurement.

The situation today has not significantly changed from what existed in the mid-1970's. The primary problem has been establishing the existence of a scaling law which relates the false oblateness introduced by changes in the limb-darkening function to observable properties of the measurements. Hill and Beardsley (1987) discuss the lack of an established scaling law for Princeton-type oblateness observations (see Dicke, Kuhn, and Libbrecht 1987, and references therein). The oblateness work in the mid-1970's by SCLERA also did not have a firmly established scaling law. However, the SCLERA results of Hill and Stebbins may be model independent because oblateness measurements were used only when $E = 0$. Nevertheless, two scan amplitudes yielding the same apparent differential diameters as implied by $E = 0$ does not rule out the possibility of brightness effects altering oblateness results (Hill and Stebbins 1975, and Hill, Stebbins, and Oleson 1975).

The 1983 SCLERA observations have an advantage over the work done at SCLERA in the 1970's. There are now several observables which may be used to establish the scaling law for both J_2^* and J_4^* instead of one.

To establish these observables, the left hand side of equations 4.1.3 and 4.1.4 were first calculated using the data that have been corrected for translation onto a chord. Data containing clouds and obvious active regions found using the techniques described in the

previous section were also removed. The calculations were performed for each of the four a_i 's. Next the following differences were formed.

$$\begin{aligned}
 x_1 &= \tilde{D}(a_4) - \tilde{D}(a_1) \\
 x_2 &= \tilde{D}(a_4) - \tilde{D}(a_2) \\
 x_3 &= \tilde{D}(a_4) - \tilde{D}(a_3) \\
 x_4 &= \tilde{D}(a_3) - \tilde{D}(a_1) \\
 x_5 &= \tilde{D}(a_3) - \tilde{D}(a_2) \\
 x_6 &= \tilde{D}(a_2) - \tilde{D}(a_1)
 \end{aligned}
 \tag{6.1.2}$$

and,

$$\begin{aligned}
 y_1 &= \Delta D(a_4) \sin 2(\pi P) + \Delta D_{45}(a_4) \cos 2(\pi P) - \\
 &\quad \Delta D(a_1) \sin 2(\pi P) - \Delta D_{45}(a_1) \cos 2(\pi P) \\
 y_2 &= \Delta D(a_4) \sin 2(\pi P) + \Delta D_{45}(a_4) \cos 2(\pi P) - \\
 &\quad \Delta D(a_2) \sin 2(\pi P) - \Delta D_{45}(a_2) \cos 2(\pi P) \\
 y_3 &= \Delta D(a_4) \sin 2(\pi P) + \Delta D_{45}(a_4) \cos 2(\pi P) - \\
 &\quad \Delta D(a_3) \sin 2(\pi P) - \Delta D_{45}(a_3) \cos 2(\pi P) \\
 y_4 &= \Delta D(a_3) \sin 2(\pi P) + \Delta D_{45}(a_3) \cos 2(\pi P) - \\
 &\quad \Delta D(a_1) \sin 2(\pi P) - \Delta D_{45}(a_1) \cos 2(\pi P) \\
 y_5 &= \Delta D(a_3) \sin 2(\pi P) + \Delta D_{45}(a_3) \cos 2(\pi P) - \\
 &\quad \Delta D(a_2) \sin 2(\pi P) - \Delta D_{45}(a_2) \cos 2(\pi P) \\
 y_6 &= \Delta D(a_2) \sin 2(\pi P) + \Delta D_{45}(a_2) \cos 2(\pi P) - \\
 &\quad \Delta D(a_1) \sin 2(\pi P) - \Delta D_{45}(a_1) \cos 2(\pi P) .
 \end{aligned}
 \tag{6.1.3}$$

The subscripts denoting which slits were used to form the diameter have been dropped for simplicity. However the equations found in 4.1.8 can

be solved for any of the three slit combinations that yield diameter measurements.

The x_j and y_j are next Fourier transformed and summed in the same way as the instrumental errors have been done in section 4.2. The F_k values corresponding to the brightness terms appropriate for equation 4.1.8 are listed below. These equations are an extension of 4.1.9.

Eq. 4.1.3

$$\begin{aligned} F_6 &= \\ F_7 &= \\ F_8 &= \text{FT}[x_1] \\ F_9 &= \text{FT}[x_2] \\ F_{10} &= \text{FT}[x_3] \\ F_{11} &= \text{FT}[x_4] \\ F_{12} &= \text{FT}[x_5] \\ F_{13} &= \text{FT}[x_6] \end{aligned}$$

Eq. 4.1.4

$$\begin{aligned} &\text{FT}[y_1] \\ &\text{FT}[y_2] \\ &\text{FT}[y_3] \\ &\text{FT}[y_4] \quad 6.1.4 \\ &\text{FT}[y_5] \\ &\text{FT}[y_6] \end{aligned}$$

The amplitudes associated with these terms are A_8 through A_{13} , respectively, for the associated terms in equation 4.1.3 to find J_4^* and A_6 through A_{11} , respectively, in equation 4.1.4 to find J_2^* .

Since there are four values of a_i , there can be only 3 independent brightness terms formed in the above fashion for each a_i and slit combination used on the left hand side of the equations

represented by 4.1.8. Note that even these three combinations are not completely independent because diameters based on the larger values of the scan amplitudes are always partially correlated with the smaller scan amplitudes. The closer the magnitude of the two scan amplitudes, the higher the correlation.

The brightness terms chosen for the right hand side of the equations represented by 4.1.8 are listed below for the four a_i used in the left hand side.

Solving Equations 4.1.8 for J_4^*

Scan Amplitude	Brightness Terms
a_1	$A_8^F F_8$, $A_{11}^F F_{11}$, and $A_{13}^F F_{13}$
a_2	$A_9^F F_9$, $A_{12}^F F_{12}$, and $A_{13}^F F_{13}$ 6.1.5
a_3	$A_{10}^F F_{10}$, $A_{11}^F F_{11}$, and $A_{12}^F F_{12}$
a_4	$A_8^F F_8$, $A_9^F F_9$, and $A_{10}^F F_{10}$

Solving equations 4.1.8 for J_2^*

Scan Amplitude	Brightness Terms
a_1	$A_6^F F_6$, $A_9^F F_9$, and $A_{11}^F F_{11}$
a_2	$A_7^F F_7$, $A_{10}^F F_{10}$, and $A_{11}^F F_{11}$ 6.1.6
a_3	$A_8^F F_8$, $A_9^F F_9$, and $A_{10}^F F_{10}$
a_4	$A_6^F F_6$, $A_7^F F_7$, and $A_8^F F_8$

Including the instrumental terms, there are a total of 10 free parameters describing the solution of the equations represented by 4.1.8 for J_4^* . The solution for J_2^* requires 8 free parameters.

In an effort to further reduce the magnitude of systematic errors introduced by an incorrect scaling law, one more data selection criterion has been used. If $|\bar{x}_1| > 100$ milliarcseconds, where \bar{x}_1 was the mean value of x_1 for one day of observations, then that day of observations was rejected from the least squares fit for J_4^* . Similarly if $|\bar{y}_1| > 50$ milliarcseconds, then that day's data was not used in the analysis for J_2^* . The values of \bar{x}_1 and \bar{y}_1 were chosen for this selection criterion because they should have the highest sensitivity to changes in the limb darkening function. The limits have been made as restrictive as possible without removing so much of the data as to create statistical uncertainty.

The equations in 4.1.8 were solved using the data that was "prewhitened" using the above techniques. Solutions were found for each of the three slit combinations that measure diameters. Each slit combination also had four possible solutions corresponding to the four a_i 's used in calculating the left side of the equations 4.1.8. Chapter 7 describes the results of these solutions.

CHAPTER 7

J_2^* AND J_4^* RESULTS

The original 1983 data set consisted of over 2700 sets of diameter measurements (at the four polar angles) for each of the three slit combinations. After "prewhitening" as described in chapter 6, less than 30% of the original data remained available for analysis. About 30% of the data was removed because of atmospheric phenomena and another 30% removed because of apparent limb-darkening function shape changes between the four polar angles. As previously stated, there were also two days removed from the analysis due to an unacceptably large translation correction.

Table 1 is a list of the observations that satisfy the selection criteria established in chapter 6. This list is for diameter measurements using $D_{2,5}(\theta, a_i)$. The first column represents the day numbers. On two days the data sets are divided into morning and afternoon segments because of clouds interfering around mid-day. The morning data sets are denoted by the suffix 'M' and the afternoon data sets are denoted by the suffix 'A'. The next column represents the number of sets of θ selected for each day of observations. The third column is \bar{y}_1 (daily averages) where y_1 is defined in section 6.1 and at the bottom of the table. The next column is the standard deviation of the scatter in \bar{y}_1 . The fifth and sixth columns represent analogous quantities for \bar{x}_1 and σ_{x1} respectively. The last two columns

TABLE 1

Observations used to find J_4^* and J_2^*								
	Day	Number	\bar{a}_1	σ_{y1}	\bar{x}_1	σ_{x1}	J_4^*	J_2^*
1	170	134	8	119	4	163	X	X
2	171	144	57	97	72	159	X	
3	172	41	40	85	64	107	X	X
4	177M ^d	56	7	132	29	227	X	X
5	177A	21	54	167	89	214	X	
6	178M	34	62	149	22	245	X	
7	178A	72	53	158	12	197	X	
8	179	49	5	157	16	205	X	X
9	180	142	31	150	20	204	X	X
10	181	98	6	169	85	213	X	X
11	182	140	42	128	64	170	X	X
12	183	57	64	94	38	229	X	
13	184	144	43	149	17	221	X	X
14	186	70	58	145	29	252	X	
15	187	13	25	84	28	93	X	X
16	190	29	59	98	45	146	X	
17	193	24	25	145	41	247	X	X
18	194	122	50	163	106	198		X
19	195	15	79	73	12	123	X	
20	197	112	35	144	19	184	X	X
21	198	113	43	188	82	206	X	X
22	199	22	95	91	23	67	X	
23	200	57	88	143	104	187		
24	201	19	6	117	9	190	X	X

Total number of sets of polar angles = 1728

Number of sets of polar angles used for J_4^* (J_2^*) analysis = 1549 (1207).

Number of days used for J_4^* (J_2^*) analysis = 22 (14).

a. $\bar{y}_1 = \Delta D(a_4) \sin 2(\eta - P) + \Delta D(a_4) \cos 2(\eta - P)$
 $= \Delta D(a_1) \sin 2(\eta - P) + \Delta D(a_1) \cos 2(\eta - P)$
 (daily average in milliarcseconds)

b. σ_{x1} (σ_{y1}) = standard deviation of the scatter.

c. $\bar{x}_1 = \bar{D}(a_4) + \bar{D}(a_1)$ (daily average in milliarcseconds)

d. The suffix M represents morning observations and the suffix A represents afternoon observations. The day was broken into two data sets because of clouds.

establish which days were included in the J_4^* or J_2^* analysis. An 'X' in the column under these labels signifies that the day of observations was included in the analysis. As stated previously, the total time span for the data set was 32 days.

Inspection of the table shows that the mean values of the brightness parameters vary considerably day to day. Also, σ_{x1} and σ_{y1} are over 100 milliarcseconds for most days. Although in general the brightness signal is not random and therefore cannot be described by a Gaussian distribution, σ_{x1} and σ_{y1} nevertheless are good indicators for how much the limb-darkening functions are changing over the timescale of a few hours.

Since this table was compiled after the selection criteria in the previous chapter removed the majority of brightness effects, the variability of the apparent limb-darkening functions were far greater than these mean values and standard deviations would suggest. Clearly, it will be vital for any shape investigation of the Sun to remove the effects of these limb-darkening function changes from the analysis.

7.1 Solutions for J_4^* and J_4

The coefficients in equation 4.1.3 and in 6.1.5 were found using the Fourier transform (FT) technique described in section 4.2. The frequency sampling interval ($\Delta\nu$) in equation 4.1.8 was 0.0298 μHz . Different solutions were found by varying the frequency range over which the amplitudes were summed. The number of amplitudes summed varied between $N = 2000$ and 20000; the smaller the frequency range,

the more filtering of the data was involved. The objective was to find the optimum filter to minimize the errors. This technique also showed how sensitive the solution was to a change in "N".

In an effort to increase the signal to noise ratio, a threshold amplitude α was established for the F_k 's. At least one of the 10 F_k 's had to have an amplitude greater than α for the amplitudes associated with the $j \Delta v$ ($j = 0$ to 20000) to be included in the least squares analysis. The value of α used was 2 milliarcseconds. This value has been partially optimized to reduce the error in the results. However, future improvements in the phase sensitive detection may be possible.

\bar{A}_1 vs. N is represented in Figure 8 where $\bar{A}_1(\bar{D}) = \frac{35}{16} \bar{J}_4^*$ and $\bar{J}_4^* = [\sum_{i=1}^4 J_4^*(a_i)]/4$. The diameter measurements corresponding to $\bar{D}_{2,5}$ are used in the analysis. The vertical axis is measured in milliarcseconds and the horizontal axis represents the number (N) of Δv over which the FT is summed. The errors in the figure are

$\bar{\sigma}_{A1} = [\sum_{i=1}^4 \sigma_{A1}(a_i)]/4$, where $\sigma_{A1}(a_i)$ is the error associated with the coefficient evaluated using scan amplitude a_i . $\bar{\sigma}_{A1}$ is used to represent the error of the coefficient because of the high correlation between the results using different a_i . This estimate slightly overestimates the true one sigma error.

The figure shows that systematic errors are probably altering A_1 when $N < 4000$. This may be caused by an insufficient number of large amplitude harmonics in the F_k to allow a statistically significant solution. Another possibility is that the F_k may not be

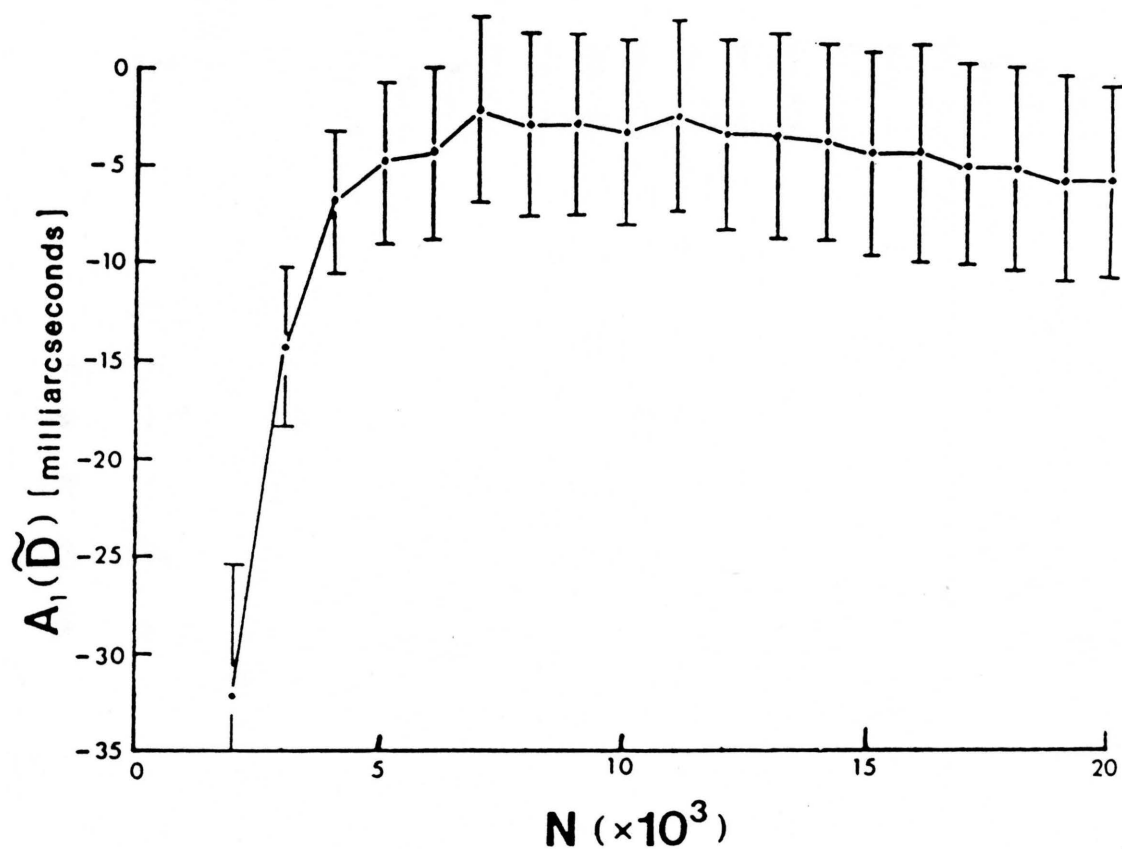


Figure 8. $\tilde{A}_1(\tilde{D})$ Vs. N .

N represents the number of amplitudes used in the harmonic analysis described by the system of equations represented in 4.1.8. The first amplitude, summed in 4.1.8, corresponds to zero frequency and the last to $(N-1) \Delta\nu$, where $\Delta\nu = 0.0298 \mu\text{Hz}$. $\tilde{A}_1(\tilde{D}) = \frac{35}{16} \tilde{J}_4$, as defined in equations 4.1.8 and 4.1.10.

Table 2

Least Squares Coefficients^a for J_4^*

Scan # → Coef. ↓	1	2	3	4	ave
A_1	-4.6 ± 4.3	-6.1 ± 4.1	-4.3 ± 4.0	-3.7 ± 4.8	-4.6 ± 4.3
A_2	5.5 ± 10.9	-1.0 ± 10.9	2.7 ± 11.1	0.5 ± 12.6	1.9 ± 11.4
A_3	9.4 ± 5.3	10.1 ± 5.4	10.2 ± 4.5	13.4 ± 5.4	10.8 ± 5.2
A_4	-16.4 ± 6.2	-13.3 ± 6.1	-15.4 ± 6.0	-17.2 ± 6.9	-15.6 ± 6.3
A_5	-9.0 ± 5.6	-4.2 ± 6.1	-6.3 ± 6.0	-5.9 ± 7.1	-6.4 ± 6.2
A_6	23.1 ± 6.4	20.0 ± 6.5	21.4 ± 5.9	17.8 ± 6.8	20.6 ± 6.4
A_7	-1.4 ± 5.2	-3.2 ± 5.5	-2.5 ± 5.2	0.8 ± 5.5	-1.6 ± 5.4
A_8	0.09 ± 0.29			-0.03 ± 0.36	
A_9		0.06 ± 0.30		1.10 ± 0.59	
A_{10}			0.07 ± 0.22	-0.33 ± 0.54	
A_{11}	-0.14 ± 0.56		0.03 ± 0.31		
A_{12}		-0.26 ± 0.58	0.93 ± 0.52		
A_{13}	-1.10 ± 0.50	0.18 ± 0.29			

Definitions

$A_1 = \frac{35}{16} J_4^*$	Apparent \tilde{D}
$A_2 = \frac{35}{16} C_4 \cos 4\phi_1$	M_1 term
$A_3 = -\frac{35}{16} C_4 \sin 4\phi_1$	M_1 term
$A_4 = \frac{35}{16} D_4 \cos 4\phi_2$	M_2 term
$A_5 = -\frac{35}{16} D_4 \sin 4\phi_2$	M_2 term
$A_6 = \frac{35}{16} E_4 \cos 4\phi_d$	Detector term
$A_7 = -\frac{35}{16} E_4 \sin 4\phi_d$	Detector term

Table 2 continued

A_8 is coefficient of $\tilde{D}(a_4) - \tilde{D}(a_1)$	Brightness term
A_9 is coefficient of $\tilde{D}(a_4) - \tilde{D}(a_2)$	Brightness term
A_{10} is coefficient of $\tilde{D}(a_4) - \tilde{D}(a_3)$	Brightness term
A_{11} is coefficient of $\tilde{D}(a_3) - \tilde{D}(a_1)$	Brightness term
A_{12} is coefficient of $\tilde{D}(a_3) - \tilde{D}(a_2)$	Brightness term
A_{13} is coefficient of $\tilde{D}(a_2) - \tilde{D}(a_1)$	Brightness term

a. The instrumental and oblateness coefficients are listed in milliarcseconds and the brightness coefficients are dimensionless.

independent for this bandpass (because of similarities in the amplitudes of the harmonics at the lower frequencies between the various theoretical terms) making a unique solution impossible.

The solution at $N = 4000$ has the minimum one sigma error and the solutions gradually show increasing errors as N is changed in either direction. Since $N = 4000$ is near the location where low frequency systematic errors are apparently affecting results, the solution at $N = 6000$ will be adopted for A_1 . The value is $\sim 4.6 \pm 4.3$ milliarcseconds or $\bar{J}_4^* = -2.1 \pm 2.0$ milliarcseconds. Adopting a value of $\bar{\theta} = 1890$ arcseconds appropriate for observations taken around July 1, 1983 and using the value of $J_4^!$ found in chapter 2, $J_4 = 1.7 \times 10^{-6}$. The error in J_4 is discussed below. Table 2 shows all of the solar, instrumental, and brightness parameters used in the least squares analysis for $N = 6000$.

\bar{J}_4^* found using $\bar{D}_{1,4}$ and $\bar{D}_{3,6}$ are statistically several times more uncertain because of the large amount of data that had to be removed from the analysis due to changes in the limb-darkening function. They are also far more likely to contain systematic errors due to improper scaling of the brightness parameters. Therefore, these measurements are not included in the analysis.

There are several sources of error associated with the estimate of J_4 . The first of the three dominant sources is the statistical errors associated with J_4^* in the least squares fit. The next is the systematic error resulting from the chordal correction found in section 5.4. The third source is a possible systematic error due to the

brightness parameters not scaling with the false J_4^* created by limb-darkening function changes.

The resulting uncertainty in J_4 due to the first two are easy to calculate. Using the statistical error for \bar{A}_1 (4.3 milliarcseconds) and the systematic chordal correction error found in section 5.4 ($\sigma_{cd} = 1.5$ milliarcseconds), $J_4^* = -2.1 \pm 2.1$ milliarcseconds and $J_4 = (1.7 \pm 1.1) \times 10^{-6}$ (cf equation 4.1.2).

The systematic error resulting from changes in the limb-darkening function is much more difficult to estimate. Since these errors are similar for both J_2 and J_4 a discussion of these effects will be deferred until chapters 8 and 9.

J_4 and J_4^* found above uses data that have been corrected for translation onto a chord. If the same analysis is performed using the uncorrected data set, $J_4^* = -5.8 \pm 1.2$ milliarcseconds. Correcting this result by subtracting $\frac{16}{35} \bar{d}$ found from equation 5.4.4, $J_4^* = -3.3 \pm 1.4$ milliarcseconds. This value is very similar to the value obtained using the corrected data set. However the error associated with it is slightly smaller. Apparently the chord correction is adding noise to the data, although, this noise has little affect on the solution. J_4^* and J_4 found from the corrected data set will be the adopted solutions.

7.2 Solutions for J_2^* and J_2

Solutions for J_2^* were found using equation 4.1.4 and the brightness terms listed in 6.1.6. The value of α was once again 2 milliarcseconds for the eight parameter least squares analysis. In Figure 9 is displayed values of \bar{A}_1 vs. N, where $\bar{A}_1(\Delta D) = -(\frac{3}{2} \bar{J}_2^* + \frac{5}{8} \bar{J}_4^*)$. The figure represents the solution for the diameter measurements using $D_{2,5}$. The \bar{A}_1 found from $D_{1,4}$ and $D_{3,6}$ were, once again, statistically several times less reliable because of limb-darkening function changes and, therefore, not used to determine J_2^* or J_2 .

The minimum one sigma uncertainty of the coefficient occurs at $N = 13000$ with the error gradually increasing as N changes from this value. The figure shows a downward bias in \bar{A}_1 as N is increased. This suggests that systematic errors are affecting at least part of the amplitudes in the frequency ranges considered. $\bar{A}_1 = 27.5 \pm 1.6$ milliarcseconds for $N = 9000$ will be adopted as the best estimate because the one sigma error associated with this amplitude shows a better overlap with the possible values of \bar{A}_1 on the figure. It has a slightly larger error than the amplitude at $N = 13000$. All solar, instrumental, and brightness terms associated with the J_2^* solution for $N = 9000$ are listed in Table 3.

Using J_2' found from equation 2.23, the chordal systematic error of 2.0 milliarcseconds found from equation 5.4.4, and \bar{J}_4^* found above, $\bar{J}_2^* = -17.4 \pm 1.9$ milliarcseconds and $J_2 = (3.4 \pm 1.0) \times 10^{-6}$

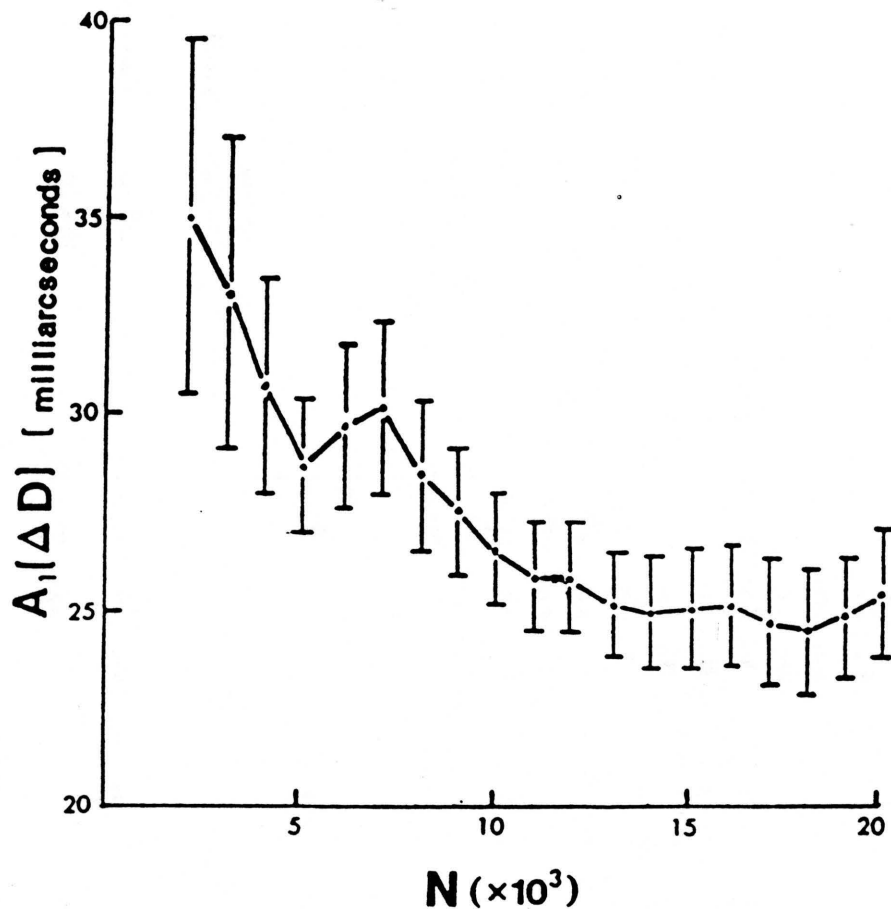


Figure 9. $\bar{A}_1(\Delta D)$ Vs. N .

N represents the number of amplitudes used in the harmonic analysis described by the system of equations represented in 4.1.8. The first amplitude, summed in 4.1.8, corresponds to zero frequency and the last to $(N-1)\Delta\nu$, where $\Delta\nu = 0.0298 \mu\text{Hz}$. $\bar{A}_1(\Delta D) = -(\frac{3}{2}\bar{J}_2 + \frac{5}{8}\bar{J}_4)$, as defined in equations 4.1.8 and 4.1.10.

Table 3

Least Squares Coefficients^a for J_2^*

Scan # → Coef. ↓	1	2	3	4	ave
A_1	26.4 ± 1.6	26.1 ± 1.2	28.3 ± 1.8	29.3 ± 1.7	27.5 ± 1.6
A_2	2.6 ± 4.4	3.8 ± 4.3	3.2 ± 4.7	1.4 ± 4.8	2.8 ± 4.6
A_3	91.2 ± 17.5	86.1 ± 16.7	94.1 ± 18.8	99.7 ± 18.2	92.8 ± 17.8
A_4	-159.0 ± 3.4	-157.7 ± 3.2	-159.4 ± 3.7	-160.2 ± 3.9	-159.1 ± 3.6
A_5	-82.4 ± 4.4	-83.3 ± 4.7	-79.0 ± 4.3	-79.1 ± 4.7	-81.0 ± 4.5
A_6	-0.02 ± 0.07			0.17 ± 0.09	
A_7		-0.02 ± 0.08		0.38 ± 0.15	
A_8			-0.05 ± 0.07	0.41 ± 0.15	
A_9	-0.46 ± 0.14		0.18 ± 0.09		
A_{10}		-0.41 ± 0.15	0.40 ± 0.13		
A_{11}	-0.38 ± 0.12	0.13 ± 0.07			

Definitions

$A_1 = -(\frac{3}{2} J_2^* + \frac{5}{8} J_4^*)$	Apparent Oblateness
$A_2 = (\frac{3}{2} D_2 + \frac{5}{8} D_4) \sin 2\phi_2$	M_2 term
$A_3 = -(\frac{3}{2} D_2 + \frac{5}{8} D_4) \cos 2\phi_2$	M_2 term
$A_4 = (\frac{3}{2} E_2 + \frac{5}{8} E_4) \sin 2\phi_d$	Detector term
$A_5 = -(\frac{3}{2} E_2 + \frac{5}{8} E_4) \cos 2\phi_d$	Detector term
A_6 is coefficient of $f(a_4) = f(a_1)$	Brightness term
A_7 is coefficient of $f(a_4) = f(a_2)$	Brightness term
A_8 is coefficient of $f(a_4) = f(a_3)$	Brightness term
A_9 is coefficient of $f(a_3) = f(a_1)$	Brightness term

Table 3 continued

A_{10} is coefficient of $f(a_3) \approx f(a_2)$	Brightness term
A_{11} is coefficient of $f(a_2) \approx f(a_1)$	Brightness term

$$f(a_i) = \Delta D(a_i) \sin 2(\eta \mp P) + \Delta D_{45}(a_i) \cos 2(\eta \mp P)$$

a. The instrumental and oblateness coefficients are listed in milliarcseconds and the brightness coefficients are dimensionless.

(cf eq. 4.1.2). Using the data set uncorrected for translations in the least squares analysis and then correcting \bar{J}_2^* with the results from equation 5.4.4, $\bar{J}_2^* = 16.0 \pm 1.9$ milliarcseconds. This is similar to the results using the corrected data set. Once again the solution for the corrected data set will be the adopted solution.

The errors quoted for J_2^* and J_2 assume $A_1(\Delta D)$ and $A_1(\tilde{D})$ are uncorrelated and that the brightness parameters correctly describe the effects of the false oblateness. The errors associated with $A_1(\Delta D)$ and $A_1(\tilde{D})$ can be shown to be partially correlated by first writing J_2^* in terms of the coefficients:

$$J_2^* = \frac{2}{3} [\bar{A}_1(\Delta D) + \frac{2}{7} \bar{A}_1(\tilde{D})] \quad . \quad 7.2.1$$

The equation shows that the coefficients are correlated if ΔD and \tilde{D} are correlated. After the low pass filtering in section 4.2, these parameters probably are correlated because both the chordal correction and changes in the limb-darkening function are observed to alter, primarily, only equatorial diameter measurements. Since a systematic equatorial diameter change would affect ΔD and \tilde{D} by the same amount, $A_1(\Delta D)$ and $A_1(\tilde{D})$ would be altered by approximately equal amounts. However, because of the small coefficient in front of the second term, a negligible difference in the error results, regardless of whether the errors are treated as correlated or uncorrelated.

7.3 Atmospheric Effects

In section 4.1 it was demonstrated that if the distortion of the solar image due to differential refraction can be described by the P_2 term of a Legendre series, then differential refraction could not introduce systematic errors into J_2 or J_4 . Section 4.1 also shows that this is probably a very good assumption.

There were two tests performed during the data analysis for J_2^* to check for an improperly described differential refraction. The first test involved the $[\Delta D_{45} \cos 2(\eta-P)]$ -term used in equation 4.1.4. If this term properly removed differential refraction, then all $\cos 2(\eta-P)$ dependence on the right hand side of the equation should be removed. By adding an $[\bar{A}_{12}(\Delta D) \cos 2(\eta-P)]$ -term on the right hand side of the equation and treating the coefficient as a least squares parameter, a test for residual differential refraction could be performed. With $N = 9000$ and $\alpha = 2$ milliarcseconds, the following values of $\bar{A}_1(\Delta D)$ and $\bar{A}_{12}(\Delta D)$ were found:

$$\begin{aligned}\bar{A}_1(\Delta D) &= 27.0 \pm 1.6 & 7.3.1 \\ \bar{A}_{12}(\Delta D) &= 7.2 \pm 6.6\end{aligned}$$

milliarcseconds. The value of $A_1(\Delta D)$ is almost identical to the results in the previous section (27.5 ± 1.6 milliarcseconds). Also the value of $\bar{A}_{12}(\Delta D)$ is consistent with a null value. Therefore, the $[\Delta D_{45} \cos 2(\eta-P)]$ -term probably does remove most of the systematic error associated with differential refraction. If a horizontal

component of the differential refraction is altering results as suggested in section 4.1, then it is very unlikely that $\vec{A}_{12}(\Delta D)$ would be this small.

A second test can be made to check either for a horizontal differential refraction component or for anisotropic seeing. In both cases the minor axis of the distortion may be fixed with respect to a preferred direction in the sky. This distortion would rotate as $-AZ$ with respect to the zenith direction projected down onto the solar image.

Adding the two terms, $A_{13}(\Delta D) \cos(-2 AZ)$ and $A_{14}(\Delta D) \sin(-2 AZ)$ into equation 4.1.4, the amplitude of these terms and their affect on $\vec{A}_1(\Delta D)$ can be evaluated. The results for the ten parameter least squares fit with $N = 9000$ and $\alpha = 2$ milliarcseconds are

$$\begin{aligned}\vec{A}_1(\Delta D) &= 28.1 \pm 3.0 \\ \vec{A}_{13}(\Delta D) &= -5.5 \pm 40.3 & 7.3.2 \\ \vec{A}_{14}(\Delta D) &= -10.8 \pm 32.7\end{aligned}$$

milliarcseconds. Once again there is no evidence to support the existence of a systematic error resulting from an incorrectly removed differential refraction or anisotropic seeing.

CHAPTER 8

SOLAR PHENOMENA AND THE MULTIPOLE MOMENTS

Of the several types of phenomena that are known to occur near the surface of the Sun, only a few can introduce systematic errors into SCLERA-type observations.

The narrow bandpass filters (centered at 550 nm in the solar continuum), which are located above the solar detectors, prevent most chromospheric activity from interfering with observations. The FFTD as defined in equation 3.2.1 is also insensitive to a scaling change in the intensity profile $[I(\theta, \mu, t)]$ of the solar limb.

The effects of solar rotation, magnetic fields, velocity fields, and other surface stresses can all be calculated using the formalism developed in Chapter 2. Currently, only solar rotation is believed to contribute significantly to apparent oblateness results (Dicke 1970, Dicke and Goldenberg 1974, Dicke et al. 1985, 1986, 1987), and this contribution has been calculated.

Active regions are also easy to identify and remove from the data analysis. In Figure 7 is shown an example of this type of detection.

One source of false oblateness that could create a systematic error results from the possibility that the μ dependence of $I'(\mu, t) = I(\theta_a, \mu, t) - I(\theta_b, \mu, t)$ could change in such a way that the false oblateness generated by I' does not scale with the observables

established in chapter 6. Here, θ_a and θ_b refer to any two polar angles.

A second possible source of a systematic error that could be important would be an intrinsic oblateness that varied over the time-scale of the observations. The data window may then create misleading results. These two types of systematic errors are addressed in the next two sections.

8.1 Systematic Errors from Changes in I'

Section 6.1 shows the brightness parameter used by Hill and Stebbins (1975) in their oblateness work. The value of $\Delta d_e/E = 0.46 \pm 0.25$ found from their observations was consistent with what was expected applying the FFTD theory to several brightness models that existed at that time (Durney and Roxburgh 1969; Chapman and Ingersoll 1972; Ingersoll and Spiegel 1971; Durney and Werner 1971; Durney 1973). This result can be compared with the brightness coefficients found in chapter 7. Because the current analysis uses several brightness parameters, a direct comparison is difficult to interpret. The interpretation is clearer if the least squares analysis described in chapter 4 is modified.

Equations 4.1.3 and 4.1.4 can be rearranged such that all of the instrumental and solar shape terms are on the left hand side of the equations with the mean values of the coefficients found in tables 2 and 3 used for the A_k . Only one brightness coefficient and no

instrumental or shape coefficients will be determined using the FT-least squares analysis. The modified equations are of the form:

$$[\bar{D}(a_h) \sim \sum_{k=1}^7 A_k(\bar{D}) X_k] \sim \bar{Q}_h^4 = R_{h,i,j}^4 \{[\bar{D}(a_i) \sim \bar{D}(a_j)] \sim \bar{U}_{i,j}^4\} \quad 8.1.1$$

$$[f(a_h) \sim \sum_{k=1}^5 A_k(\Delta D) Y_k] \sim \bar{Q}_h^2 = R_{h,i,j}^2 \{[f(a_i) \sim f(a_j)] \sim \bar{U}_{i,j}^2\} \quad 8.1.2$$

where X_k (Y_k) are the terms found within the square brackets in the equations represented by 4.1.9. \bar{Q}_h^4 and $\bar{U}_{i,j}^4$ (\bar{Q}_h^2 and $\bar{U}_{i,j}^2$) represent the mean values of the quantity in square brackets on the left and right hand sides of equation 8.1.1 (8.1.2), respectively. $R_{h,i,j}^4$ and $R_{h,i,j}^2$ are the least squares coefficients to be found using the FT-technique described in section 4.2. The quantity $f(a_h)$ represents the expression on the left side of equation 4.1.4. It is also defined at the end of table 3.

The coefficients of the brightness terms are determined independently from all other brightness terms when equations 8.1.1 and 8.1.2 are solved for each of the 24 values of R_4 and R_2 . Tables 4 and 5 are a list of these coefficients. The equations are solved with the implicit assumption that the instrumental and solar shape terms are known perfectly. As a result of this assumption, there may be a systematic error in the brightness coefficients that has not been represented by the error listed with the coefficients. This systematic error should be minimal because of the small errors associated with the instrumental and solar shape coefficients. Also, the harmonics

generated in the spectrum by the brightness terms (using the FT→Least Squares technique) are substantially independent from the instrumental and solar shape terms.

Further simplifying the notation, let

$$\tilde{D}b_h = R^4_{h,i,j} Xb_{i,j} \quad 8.1.3$$

and

$$\Delta Db_h = R^2_{h,i,j} Yb_{i,j} \quad 8.1.4$$

represent equations 8.1.1 and 8.1.2, respectively. In this notation $\tilde{D}b_h$ (ΔDb_h) is the observed brightness and $Xb_{i,j}$ ($Yb_{i,j}$) represents the brightness term on the right hand side of equation 8.1.3 (8.1.4). Since $\tilde{D}b_h$ (ΔDb_h) is a function of scan amplitude, $R^4_{h,i,j}$ ($R^2_{h,i,j}$) can be plotted as a function of scan amplitude. In Figures 10 and 11 are plotted values of $R^4_{h,4,1}$ vs. "a" and $R^2_{h,4,1}$ vs. "a", respectively. Other pairs of the indices (i,j) can be used to form similar plots, but they all appear qualitatively similar so only these will be displayed.

The figures and tables show a number of interesting features. First, a strong correlation exists between R^4 and R^2 . Because of the complicated nature of the functions, brightness effects would reduce the correlation if the limb darkening functions associated with $D(45)$ or $D(-45)$ are significantly varying. If $D(0)$ is the apparent diameter that is being altered by brightness effects, then R^4 and R^2 would be of opposite sign because of the way the diameters are added and subtracted in ΔD and \tilde{D} .

This correlation can only be understood if most of the brightness effects are occurring at the equator. The correlation agrees with the qualitative results found in chapter 6 from looking at $D(-\theta, a_j) - D(-\theta, a_i)$ vs time for each day of data.

It can be shown, algebraically, that $R_{j,i,j} = 1 + R_{i,i,j}$. This constraint specifies the slope between the endpoints on the figures. This slope is $S_{4,1} = 1/(a_4 - a_1)$. Equivalently, it can be said that the endpoints of the figures are not independent points. The plotted coefficients that are not on the endpoints of the figures have no constraints and their locations are a function of the FFTD edge definition operating on I' . Within the uncertainties on the coefficients, the figures show an approximately linear relationship existing between the brightness coefficients and the scan amplitude used to determine the quantities Δb_n and $\bar{D}b_n$. This linearity implies that the effects of I' on $A_1(\Delta D)$ and $A_1(\bar{D})$ are probably well described by the brightness parameters and coefficients used in the shape analysis in chapter 7. Variations from this linear relationship would indicate a complex form of I' which could produce errors in the shape analysis.

The figures also show that I' is in such a form that the false oblateness generated from a large scan amplitude such as a_4 (21.5 arcseconds) is of the opposite sign and of approximately equal magnitude as that created from synthesizing a small scan amplitude such as a_1 (~ 5.4 arcseconds). This fortuitous behavior of I' and the FFTD's high sensitivity to this type of change in limb-darkening

TABLE 4

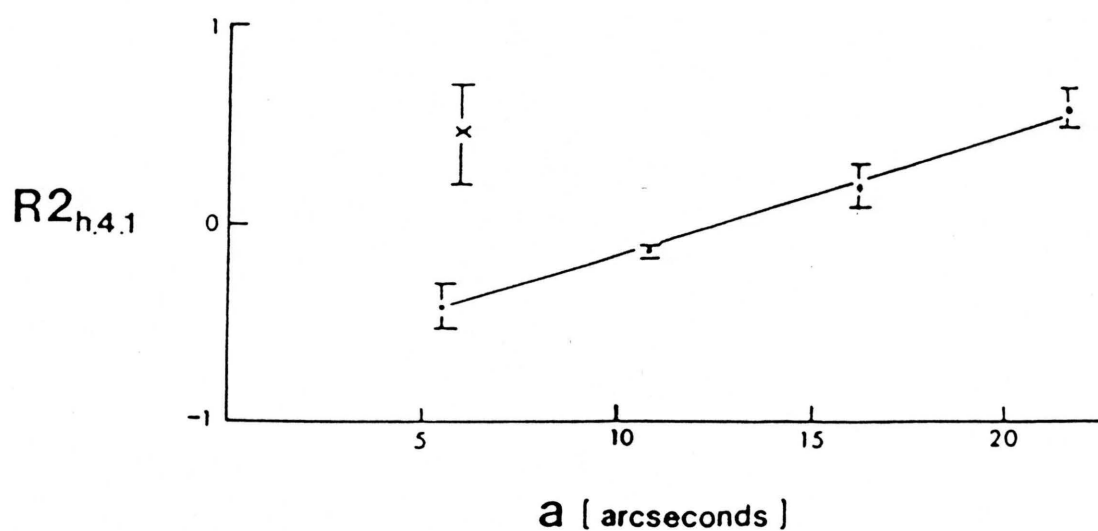
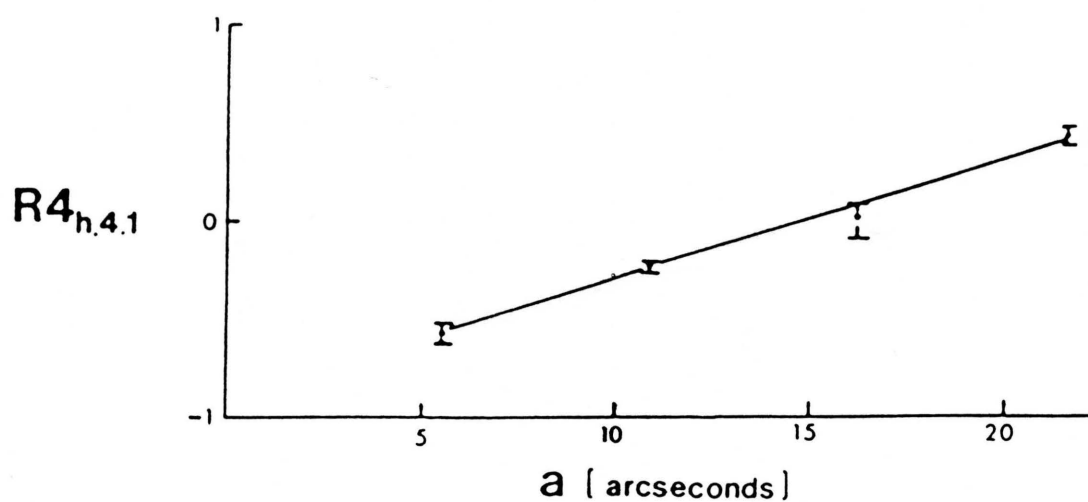
Values of the Brightness Coefficients $R^4_{h,i,j}$

$h \rightarrow$ $i,j \downarrow$	1	2	3	4
2,1	-0.97 ± 0.06	0.03 ± 0.06	0.07 ± 0.20	-0.04 ± 0.08
3,1	-0.71 ± 0.09	-0.11 ± 0.01	0.29 ± 0.09	0.19 ± 0.01
4,1	-0.56 ± 0.03	-0.21 ± 0.02	0.02 ± 0.08	0.44 ± 0.03
3,2	-0.39 ± 0.14	-0.34 ± 0.07	0.66 ± 0.05	0.58 ± 0.11
4,2	-0.29 ± 0.01	-0.33 ± 0.00	0.00 ± 0.01	0.67 ± 0.00
4,3	-0.21 ± 0.06	-0.30 ± 0.04	-0.34 ± 0.05	0.66 ± 0.05

TABLE 5

Values of the Brightness Coefficients $R^2_{h,i,j}$

$h \rightarrow$ $i,j \downarrow$	1	2	3	4
2,1	-0.83 ± 0.04	0.18 ± 0.03	-0.04 ± 0.05	-0.24 ± 0.18
3,1	-0.68 ± 0.01	-0.08 ± 0.04	0.33 ± 0.02	0.21 ± 0.27
4,1	-0.41 ± 0.11	-0.13 ± 0.02	0.20 ± 0.10	0.59 ± 0.10
3,2	-0.23 ± 0.07	-0.40 ± 0.03	0.61 ± 0.03	0.73 ± 0.29
4,2	0.03 ± 0.10	-0.24 ± 0.02	0.19 ± 0.08	0.77 ± 0.02
4,3	0.11 ± 0.24	-0.16 ± 0.01	-0.07 ± 0.17	0.93 ± 0.18



Figures 10 and 11. $R4_{h,4,1}$ and $R2_{h,4,1}$ Vs. Scan Amplitude.

These brightness coefficients are defined in equations 8.1.3 and 8.1.4, respectively. In Figure 11 the symbol X represents a related brightness coefficient ($\Delta d_e/E$) found by Stebbins (1975).

function produces the relatively small values of R_4 and R_2 found on the figures and in the tables.

The form of I' that apparently was in operation during 1983 is also supported by differential radius observations taken in 1979 (Bos 1982). Hill, Alexander, and Caudell (1985) using the 1979 observations analyzed the horizontal spatial properties of I' produced by low-order, low-degree acoustic modes of the Sun. For certain values of the azimuthal order of the spherical harmonics Y_l^m describing the spatial properties of the oscillation, the oscillation was shown to create an apparent shape change that could be of either sign, depending on the magnitude of the scan amplitude. The results displayed in Figures 10 and 11 also show this behavior.

The value of $\Delta d_e/E$ found from Stebbins (1975) is also plotted on Figure 11. The value of $\Delta d_e/E$ should be approximately equal to $R_{2,4,1}$ if I' has not changed during the time between the two studies. The value of his coefficient is $\Delta d_e/E = 0.46 \pm 0.25$. The current work has $R_{2,4,1} = -0.41 \pm 0.11$. The two studies do not even agree in sign. This may indicate that a change in the μ dependence of I' has occurred during the ten years between the two analyses. However, it is very likely that the apparent difference in I' is a result of the difference in which the effects of solar oscillations enter in the 1973 and 1983 observations. Hill and Stebbins (1975) could not simulate the a_k from recorded limb profiles. They first found ΔD using one scan amplitude and then later found it using another by changing the amplitude of the scan introduced into the servo loop. Since the observations were

performed several minutes apart, the brightness parameter could incorrectly model the false oblateness for solar oscillations with a period of around 5 minutes. In general, there would be low correlation between Δd_e and E (cf section 6.1) for solar oscillations with periods less than 10 or 15 minutes. Therefore, Hill and Stebbins (1975) were measuring the correlation between longer period changes in the limb darkening functions and the false oblateness.

With 1983 SCLERA type observations, all of the diameters calculated for a given time using the a_k originate from the same limb profile. As a result, $Xb_{i,j}$ and $Yb_{i,j}$ are a measure of the oscillatory contribution from I' as well as a possible static or slowly varying component found by Hill and Stebbins (1975). Since the oscillating contribution can alter $R^2_{h,i,j}$ and $R^4_{h,i,j}$, it is not necessarily expected that the brightness coefficient found from Stebbins should agree with this work.

It is impossible to prove that the μ dependence of I' did not change during the observing period in such a way as to create a false oblateness that is undetectable with the current technique. However, because of the observed high sensitivity of the FFTD to apparent changes in the limb darkening functions and the use of several brightness parameters to minimize the possibility of any false oblateness not scaling with the observables, it seems unlikely that a large uncorrected systematic brightness term is altering either J_2^* or J_4^* . To create a systematic error, I' must be more complex than the displays in figures 10 and 11 suggest. Also, the small σ 's associated

with the brightness coefficients show that the linear model is well representing the false oblateness that is assumed to be produced by solar oscillations.

8.2 Solid Body Distortions of the Solar Surface

A variable component of the solar oblateness on the time-scale of a few days or longer could bias the results of J_2^* and J_4^* . A preliminary search for such variability has been undertaken. The shape terms in equations 4.1.2 and 4.1.3 have been modified by adding a sinusoidally varying amplitude to the shape coefficients. The shape coefficients become:

$$J_4^* = J_4^0 + j_4^* \cos 2\pi vt + \tilde{j}_4^* \sin 2\pi vt$$

and

$$J_2^* = J_2^0 + j_2^* \cos 2\pi vt + \tilde{j}_2^* \sin 2\pi vt ,$$

where J_2^0 and J_4^0 represent the static shape terms and j_4^* , \tilde{j}_4^* , j_2^* , and \tilde{j}_2^* represent the amplitudes associated with the synodic frequency v . Unfortunately, the addition of these terms into the FT least squares analysis increased significantly the size of the residuals from the fit. All of the other parameters added to the solutions decreased the size of these residuals, giving confidence that our technique was producing the desired result. This suggested that there were now too many parameters for the analysis to derive a unique solution. Therefore, no quantitative results are available at this time.

However, statistically significant amplitudes appear to occur at $\nu = 0.44, 0.88, \text{ and } 1.76 \text{ } \mu\text{Hz}$. The amplitudes are also apparently about the same order of magnitude as the static shape term for J_2^* . These results are consistent for numerous values of "N" used in finding the solutions for the equations represented by 4.1.7. This suggests that the result is not an artifact of the data analysis.

Even stronger evidence for their existence was found by doing the least squares analysis using $D_{1,4}(-\theta, a_i)$ and $D_{3,6}(-\theta, a_i)$. These diameters appeared to be too badly contaminated by active regions to be of use in determining the static shape parameters. However, the least squares analysis produced statistically significant amplitudes at the same frequencies as found for the analysis using $D_{2,5}(-\theta, a_i)$, although the phases were different.

The systematic error introduced into J_2^* and J_4^* by the variable components has not been determined because of the instability of the solutions. However, because of the relatively short data set a several milliarcsecond error in J_2^* and J_4^* is possible if the amplitudes describing the variable components are as large as the analysis suggested.

CHAPTER 9

CONCLUSIONS

All sources of statistical and systematic errors have been listed in tables 6 and 7 for J_4^* and J_2^* , respectively. The best estimates of J_4 and J_2 are also listed. The statistical and systematic errors resulting from the instrument and terrestrial atmosphere are probably small and not a major source of error.

The uncertainty in the multipole moments due to false oblateness created by I' is a more serious problem. However, the scaling parameters used in this work should minimize the magnitude of an error created by this effect. Future work synthesizing more scan amplitudes may allow the functional form of I' to be found through the use of the FFTD formalism developed in Hill, Stebbins, and Oleson (1975). Detailed observational knowledge of I' has not been available in past oblateness studies. The additional information concerning the functional form of I' may remove the remaining scaling uncertainties encountered in this work.

The possibility of surface distortions also introduce some uncertainty in the current work, if they exist. Evidence for statistically significant amplitudes have been found at synodic frequencies of $\nu = 0.44, 0.88, \text{ and } 1.76 \text{ } \mu\text{Hz}$. These frequencies are in good agreement with the harmonic structure found by Hill and Czarnowski (1987) analyzing fine structure multiplet splittings. The $\nu = 0.88$ and

TABLE 6

 J_4^* and J_4 Results

Formal Statistical value for $\vec{A}_1(\tilde{D})$	-4.6 ± 4.3 marcsec
Uncorrected chord error	± 1.5
Scan amplitude scaling error	± 0.04
All other instrumental systematic errors	± 0.1
Scaling error due to I'	?
Error resulting from variable J_4^*	?
Best estimate of $\vec{A}_1(\tilde{D})$	-4.6 ± 4.6 marcsec
Best estimate of J_4^*	-2.1 ± 2.1 marcsec
Best estimate of J_4'	-0.6×10^{-6}
Best estimate of J_4	$(1.7 \pm 1.1) \times 10^{-6}$

Definitions

$$\vec{A}_1(\tilde{D}) = \text{Solar contribution to } \tilde{D}$$

$$\tilde{D} = D(0) + D(-90) - D(45) - D(-45)$$

$$D(\theta) = \text{Observed relative diameter at polar angle } \theta$$

$$J_4^* = \frac{16}{35} \vec{A}_1(\tilde{D})$$

$$J_4' = \text{Surface stress contribution to } J_4$$

$$J_4 = - (J_4^*/\tilde{\theta}) + J_4'$$

$$\tilde{\theta} = \text{Angular diameter of solar image for July 1, 1983}$$

$$(1890 \text{ arcseconds})$$

TABLE 7

 J_2^* and J_2 Results

Formal Statistical value for $\tilde{A}_1(\Delta D)$	27.5 ± 1.6 marcsec
Uncorrected chord error	± 2.0
Scan amplitude scaling error	± 0.26
All other instrumental systematic errors	± 0.2
Scaling error due to I'	?
Error resulting from variable J_2^*	?
Best estimate of $\tilde{A}_1(\Delta D)$	27.5 ± 2.6 marcsec
Best estimate of J_2^*	-17.4 ± 1.9 marcsec
Best estimate of J_2'	5.8×10^{-6}
Best estimate of J_2	$(3.4 \pm 1.0) \times 10^{-6}$

Definitions

$\tilde{A}_1(\Delta D)$ = Observed solar contribution to ΔD

$$\Delta D = D(+90) - D(0)$$

$D(\theta)$ = Observed relative diameter at polar angle θ

$$J_2^* = -\frac{2}{3} [\tilde{A}_1(\Delta D) + \frac{2}{7} \tilde{A}_1(\tilde{D})]$$

J_2' = Surface stress contribution to J_2

$$J_2 = - (J_2^* / \tilde{\theta}) + J_2'$$

$\tilde{\theta}$ = Angular diameter of solar image for July 1, 1983

(1890 arcseconds)

1.76 μHz frequencies are similar to frequencies found by Dicke (1981) who analyzed 1966 Princeton-type oblateness observations, and Dicke, Kuhn, and Libbrecht (1985 and 1987) who used 1983 and 1985 Princeton-type oblateness observations (the harmonic pattern was not apparent in 1984 Princeton-type observations). The frequencies at $\nu = 0.88$ and 1.76 μHz are also consistent with the harmonic structure found by Claverie et al. (1982) who analyzed whole disk intensity observations.

Using the rotation curve of Hill, Rabaey, and Rosenwald (1986) and assuming that $\nu = 0.44$ μHz is the fundamental frequency, the distortion may be originating at a depth somewhere in the outer convection zone of the Sun.

In Table 8, which has been updated from Hill and Rosenwald (1986), are included all values of J_2 found from published visual oblateness observations and rotational splitting studies. The value of $J_2 = (3.4 \pm 1.0) \times 10^{-6}$ found from the current work is approximately half the value found by Dicke, Kuhn and Libbrecht (1985) for the same observing season. However, part of the differences result from a P_4 -type shape contribution being removed from the current work. The values of ΔR are in better agreement. From this work $\Delta R = 13.8 \pm 1.6$ milliarcseconds $[A_1(\Delta D)/2]$. Dicke et al. (1985) found $\Delta R = 18.2 \pm 1.3$ milliarcseconds if their analysis did not include a color independent brightness parameter that scaled with their sampling aperture, and $\Delta R = 14.4 \pm 4.1$ milliarcseconds if the analysis included this term¹. Both of the Dicke et al. solutions included two other

1. These values include a ≈ 1 milliarcsecond correction discussed in Dicke, Kuhn, and Libbrecht (1986).

TABLE 8

Summary of Efforts to Determine J_2

<u>Rotational Splitting of Fine Structure^a</u>		<u>$J_2 \times 10^6$</u>	
Duvall et al. (1984)		0.17	± 0.04
Hill, Bos and Goode (1982)		5.5	± 1.3
Hill et al. (1984) ^b		4.5	
Hill, Rabaey and Rosenwald (1986) ^c		5.1	± 1.2
<u>Visual Solar Oblateness</u>	<u>T^d</u>	<u>ΔR^e</u>	
Dicke (1981) ^f	1966	42.0 \pm 2.0	22.8 \pm 2.0
Hill and Stebbins (1975)	1973	9.2 \pm 6.3	1.0 \pm 4.3
Dicke, Kuhn and Libbrecht ^g	1983	18.2 \pm 1.4	7.1 \pm 0.9
		14.4 \pm 4.1	4.4 \pm 2.7
Beardsley (1987) ^h	1983	13.8 \pm 1.3	3.4 \pm 1.0
Dicke, Kuhn; and Libbrecht (1986)	1984	5.6 \pm 1.3	-1.3 \pm 0.9
Dicke, Kuhn, and Libbrecht (1987)	1985	14.6 \pm 2.2	4.7 \pm 1.5

a. The value obtained by Gough (1982) is not included because it was based on a preliminary set of multiplet classifications which was in error (cf. Hill, 1984).

b. Based on rotational curve of Hill et al. (1984).

c. The value of 7.7 ± 1.8 for J_2 reported by Hill, Rabaey and Rosenwald (1986) has been corrected for a factor of 2/3 omitted in their analysis.

d. Year of visual oblateness observations.

e. Value of apparent equatorial - polar surface radius in milliarcseconds.

f. The original value of 23.7 ± 2.3 was found by Dicke and Goldenberg (1974).

g. Two values are given based on whether or not a certain type of systematic error is taken into account. The values listed have been corrected for a small systematic error discussed by Dicke, Kuhn, and Libbrecht (1986).

h. This value has a small J_{41} contribution removed that other oblateness studies have assumed to be zero.

brightness parameters that are functions of color differences and sampling apertures. Hill and Beardsley (1987) discuss in detail how this analysis may be insensitive to certain classes of I' resulting in an uncorrected false oblateness. However, their second solution including the color independent brightness term agrees with this work to better than one sigma. Also, it is possible that an uncorrected systematic error amounting to a few milliarcseconds, exists in the current work due to surface distortions or an incomplete description of the false oblateness caused by I' .

The 1973 value of $J_2 = (1.0 \pm 4.3) \times 10^{-6}$ found from the visual oblateness in Hill and Stebbins (1975) agrees well with the current work within the experimental errors. There is no evidence from SCLERA-type observations to support a 22 year variability in the intrinsic oblateness as suggested by Dicke, Kuhn, and Libbrecht (1985, 1986, and 1987).

The values of J_2 determined from rotational splitting fine structure vary between $J_2 = (0.17 \pm 0.04) \times 10^{-6}$ found from Duvall and Harvey (1984) to $J_2 = (5.1 \pm 1.2) \times 10^{-6}$ for Hill, Rabaey and Rosenwald (1986). The value of J_2 in this work is consistent with any of the published multiplet splitting results if an allowance is made for the possibility of a small uncorrected systematic error.

Using the observed value of $\Delta\omega$ (Shapiro et al. 1976) and equation 1.1.1 with $J_2 = (3.4 \pm 1.0) \times 10^{-6}$,

$$0.993 \pm 0.006 = \frac{1}{3}(2 + 2\gamma - \beta) \quad . \quad 9.1$$

The error represents the combination of measurement uncertainty for $\Delta\omega$ and the statistical uncertainty associated with J_2 . The result is about 1σ from the general relativistic value.

9.1 Absolute Errors from $A_1(\tilde{D})$

This is the first published result for J_4 derived from the visual solar shape and it is nearly consistent with a null value within the uncertainties as shown in table 6. If it can be shown from independent theoretical or observational evidence that J_4 should be either zero or nearly zero, then $A_1(\tilde{D})$ becomes a measure of the absolute error in $A_1(\Delta D)$ resulting from both incomplete modeling of the false oblateness and surface distortions. Since these are the two primary sources of uncertainties remaining in this thesis, the possibility of using $A_1(\tilde{D})$ as a measure of these errors greatly improves the reliability of the results for J_2 .

This situation arises from conclusions in chapters 6 and 8 concerning the location in solar latitude of these types of surface phenomena. Both sources are apparently altering only equatorial diameter measurements. Because of the way ΔD and \tilde{D} are defined, any systematic error in $D(\pm 90)$ will alter $A_1(\tilde{D})$ and $A_1(\Delta D)$ approximately the same amount¹. For example, if the value of $A_1(\tilde{D})$ is conclusively shown to be zero for the Sun by an independent technique,

1. There will be some differences because of slightly different data sets used for J_2 and J_4 . The filtering is also slightly different for the two analyses.

then 4.6 milliarcseconds must be added to $A_1(\Delta D)$. The new value of $A_1(\Delta D) = 32.1 \pm 2.6$ milliarcseconds and the corresponding value of $J_2 = (5.5 \pm 0.9) \times 10^{-6}$. This value is in very good agreement with SCLERA results from the fine structure splitting analysis (see table 8). It is also closer to the results of Dicke, Kuhn, and Libbrecht (1985) for their 1983 data set.

Calculations have not yet been completed for J_4 derived from multiplet splittings with the SCLERA rotation curve. However, it has been shown that this value is extremely small for internal rotation curves that are constant and equal to the surface rotation rate ($J_4 \sim 10^{-9}$, Ulrich and Hawkins 1981). If other viable rotation curves can be shown to produce similar values of J_4 , and it is shown that rotation is the only contribution to J_4 , then the results for J_2 from this section (5.5×10^{-6}) would be inconsistent with the J_2 derived from multiplet splitting using Doppler and whole disk intensity observations. The rotation curve from these techniques is consistent with solid body rotation (see table 8 and references in chapter 1).

9.2 Surface Stress Contributions to the Apparent Solar Shape

Although Dicke (1970) and Dicke, Kuhn, and Libbrecht (1985, 1986 and 1987) have argued that only surface rotation is an important contribution to the apparent solar shape, other significant contributions may eventually be found.

A general approach for calculating the contribution of these forces to the apparent solar shape were developed in Chapter 2 and

Appendix A. The surface stress contribution from rotation has been calculated and agrees well with the results of Dicke (1970). Other possible surface stresses such as magnetic fields or circulation currents have not yet been evaluated. However, it is relatively easy to calculate the shape perturbation for any force that can be expressed in analytic form over the surface of the Sun using the formalism described in this thesis.

9.3 Future Work

In the future, more observations are planned for SCLERA with an emphasis on both the long term variability and static oblateness of the Sun. New instrumentation on the telescope will produce an absolute diameter calibration as well as the differential measurements that have been found in the past. This new information will have important impact on the fields of Gravitational, Solar and Atmospheric Physics.

APPENDIX A

PERTURBATIONS OF EQUIPOTENTIAL SURFACES

In Chapter 2 a surface of constant gravitational potential is related to a surface of constant pressure when a perturbation such as rotation alters the mass distribution at the surface of the sun. Extra information provided by the equation of state and the radial component of the perturbed momentum equation can be used to establish the relationship between $\Delta r_{\phi,p}$, $\Delta r_{\phi,\rho}$ and $\Delta r_{\phi,T}$ when they are not equal. These three parameters represent the displacement between the perturbed equipotential surface and perturbed surfaces of constant pressure, density, and temperature, respectively.

The radial component of the linearized momentum equation can be expressed as:

$$\frac{1}{\rho} \frac{\partial P'}{\partial r} + \frac{\rho'}{\rho} \frac{\partial \Phi}{\partial r} + \frac{\partial \Phi'}{\partial r} = \frac{f_r'}{\rho} \quad . \quad \text{A.1}$$

The radial component of the perturbing force is f_r' .

This equation can be rewritten as:

$$\frac{\partial \left(\frac{P'}{\rho} + \Phi' \right)}{\partial r} + \frac{P}{\rho} \frac{d(\ln \rho)}{dr} \frac{d(\ln P)}{dr} \left[\frac{P'}{P} \frac{1}{\frac{d(\ln P)}{dr}} - \frac{\rho'}{\rho} \frac{1}{\frac{d(\ln \rho)}{dr}} \right] = \frac{f_r'}{\rho} \quad . \quad \text{A.2}$$

Next consider the two surfaces of constant P and ρ that exist before perturbing and the two surfaces of constant P and ρ after perturbing. The perturbed surfaces are displaced from the original surfaces by Δr_p and Δr_ρ respectively, where to first order,

$$\Delta r_p = - \frac{P'}{P \frac{d(\ln P)}{dr}}, \text{ and } \Delta r_\rho = - \frac{\rho'}{\rho \frac{d(\ln \rho)}{dr}} . \quad A.3$$

Equation A.2 can be used with A.3 to obtain an expression for the difference $\Delta r_{\rho,p} = \Delta r_\rho - \Delta r_p$:

$$\Delta r_{\rho,p} = \frac{1}{\frac{P}{\rho} \frac{d(\ln \rho)}{dr} \frac{d(\ln P)}{dr}} \left[\frac{f'_r}{\rho} - \frac{d(\frac{P'}{\rho} + \phi')}{dr} \right] . \quad A.4$$

This separation between the perturbed constant density and pressure surfaces can be expressed as a Legendre series

$$\Delta r_{\rho,p} = \sum_{m=0}^{\infty} b_m P_m , \quad A.5$$

where b_m are the Legendre coefficients. Using the orthogonality of the polynomials and equations 2.2.10 and 2.2.11, the coefficients can be expressed as

$$b_m = - \frac{(2m+1) \rho \Lambda_p \Lambda_\rho}{2 P} \int_0^\pi \left\{ \frac{f'_r}{\rho} - \frac{\partial (\sum_\ell a_\ell P_\ell)}{\partial r} \right\} P_m \sin \theta d\theta . \quad A.6$$

In this equation, the pressure and density scale heights are expressed as

$$\Lambda_p = \frac{1}{\frac{d(\ln P)}{dr}} \quad , \quad \Lambda_\rho = \frac{1}{\frac{d(\ln \rho)}{dr}} \quad , \quad \text{A.7}$$

respectively, and the a_ℓ are the coefficients found from equation 2.2.6. It is possible to solve equation A.6 irrespective of the form of the perturbation with the results valid as long as $|\phi'/\phi| \ll 1$.

For example, consider the special case where a perturbing force can be expressed as ρ times the gradient of a scalar function, Ψ :

$$\nabla_\perp \Psi = - \frac{f'_\perp}{\rho} \hat{\theta} \quad , \quad \text{and} \quad \nabla_r \Psi = - \frac{f'_r}{\rho} \hat{r} \quad . \quad \text{A.8}$$

$\Delta r_{\rho,p}$ can be found by inspection of the horizontal and radial components of the momentum equation represented by equations 2.2.1 and A.2. From the horizontal component of the momentum equation, Eq. 2.2.1, and Eq. A.8, we have

$$\frac{P'}{\rho} + \phi' + \psi = 0 \quad . \quad \text{A.9}$$

Therefore as a consequence of $f'_r = -\rho \nabla_r \psi$ from Eq. A.8, equation A.2 becomes:

$$\frac{\partial(\frac{P'}{\rho} + \Phi' + \psi)}{\partial r} + \frac{P}{\rho} \frac{d(\ln \rho)}{dr} \frac{d(\ln P)}{dr} \left[\frac{P'}{P} \frac{1}{\frac{d(\ln P)}{dr}} - \frac{\rho'}{\rho} \frac{1}{\frac{d(\ln \rho)}{dr}} \right] = 0, \quad A.10$$

and from equation A.9, equation A.10 becomes

$$\frac{P'}{P} \frac{1}{\frac{d(\ln P)}{dr}} - \frac{\rho'}{\rho} \frac{1}{\frac{d(\ln \rho)}{dr}} = 0, \quad A.11$$

or $\Delta r_{\rho,p} = 0$. The contribution from the integral in equation A.6 can be thought of as a departure from rotations that are conservative, expressible as a gradient of a scalar, since this term would vanish if the perturbation could be expressed as the gradient of a scalar function.

Next, consider the example of a realistic rotation curve. We need only $\Omega(R, \theta)$ and $d[a_\theta(r)]/dr$ evaluated near the surface to solve equation A.6. As already stated, there is disagreement among various groups concerning internal solar rotation. However, because of the extremely small differences that are projected for $\Delta r_{\rho,p}$, only an upper limit on $\Delta r_{\rho,p}$ is required. Equation A.6 shows that a curve with large radial gradients in the rotation coefficients will cause the second term in the equation to dominate. Therefore a rotation curve with the largest gradients should be used to establish an upper limit for $\Delta r_{\rho,p}$.

Analysis of SCLERA observations of low-order, low-degree global oscillations of the Sun has resulted in a proposed rotation curve which has a large radial gradient [$\Omega(r, \theta) \propto 1/(r^2)$ near the surface]

compared to those curves reported by independent research groups. The center of the sun, using this curve, is rotating approximately six times faster than the surface value. Also, latitudinal as well as the radial dependence of the rotation rate has been reported in the SCLERA work. Near the surface, other rotation curves show a fairly uniform or slightly decreasing rotation rate with increasing depth. Approximate scale heights are defined here for the SCLERA rotation curve by:

$$\Omega(r, \theta) = \sum_{q=0}^4 \Omega_q(R) P_q \exp((r-R)/h_q) \quad , \quad \text{A.12}$$

where $q = 2\ell$ with $\ell = 0, 1$, and 2 , $\Omega_q(R)$ are the surface rotation coefficients found in equation 2.2.13, and the h_q represent scale heights associated with the P_q coefficients.

A surface value of $h_0 \approx -R/2$ was reported in SCLERA Monograph Series No. 4 (Hill 1986). The latitudinal dependence of $\Omega(r, \theta)$ was determined from Hill et al. (1986b). A scale height of $h_2 \approx -R/22$ was inferred from their figure 2 for Ω_2 near the surface, and $h_4 \approx -R/76$ was taken from their exponential fit to the data.

Modifying equations 2.2.14 and 2.2.15 to include the radial dependence and using appropriate P , ρ , Λ_p , and Λ_ρ for $\tau \approx 0.1$ at 0.5μ wavelength (Vernazza et al. 1976), $b_2 \approx -180$ cm and $b_4 \approx -75$ cm. Therefore, surfaces of constant P and ρ depart very little from each other on the solar surface.

The separation between a perturbed surface of constant temperature and a perturbed surface of constant pressure can be found

by examining the linearized equation of state with constant mean molecular weight:

$$\frac{P'}{P} = \chi_{\rho} \frac{\rho'}{\rho} + \chi_T \frac{T'}{T} \quad , \quad \text{A.13}$$

where:

$$\chi_{\rho} = \left(\frac{\partial(\ln P)}{\partial(\ln \rho)} \right)_T \quad , \quad \text{and} \quad \chi_T = \left(\frac{\partial(\ln P)}{\partial(\ln T)} \right)_{\rho} \quad . \quad \text{A.14}$$

From equations A.13, A.3 and an equation similar to A.3 relating Δr_T to an Eulerian perturbation T' it is found:

$$\frac{d(\ln P)}{dr} \Delta r_p = \chi_{\rho} \frac{d(\ln \rho)}{dr} (\Delta r_p + \Delta r_{\rho,p}) + \chi_T \frac{d(\ln T)}{dr} (\Delta r_p + \Delta r_{T,p}) \quad \text{A.15}$$

where $\Delta r_{t,p} = \Delta r_t \sim \Delta r_p$. Solving for $\Delta r_{t,p}$ it is easy to show that

$$\Delta r_{T,p} = - \frac{\chi_{\rho}}{\chi_T} \frac{d(\ln \rho)}{d(\ln T)} \Delta r_{\rho,p} \quad . \quad \text{A.16}$$

If $\Delta r_{\rho,p} = 0$ as in the case of the perturbing force being expressed as ρ' times a gradient of a scalar function, then A.16 shows $\Delta r_{T,p} = 0$. As a consequence, $\Delta r_p = \Delta r_{\rho} = \Delta r_T$. This result is equivalent to the generalized form of Von Zeipel's theorem shown in equation 2.5.

Equations A.5, A.16 and 2.18 show for the assumed photospheric model and rotation curve that

$$|\delta r_{T,p}| \approx 7 \times |\delta r_{\rho,p}| < 10^{-3} |\delta r_{\phi,p}| \quad \text{A.17}$$

where

$$\begin{aligned} \delta r_{T,p} &= \Delta r_{T,p}(\theta_a) - \Delta r_{T,p}(\theta_b) , \\ \delta r_{\rho,p} &= \Delta r_{\rho,p}(\theta_a) - \Delta r_{\rho,p}(\theta_b) , \\ \delta r_{\phi,p} &= \Delta r_{\phi,p}(\theta_a) - \Delta r_{\phi,p}(\theta_b) , \end{aligned} \quad \text{A.18}$$

and θ_a and θ_b are any two polar angles. Equations A.17, A.18 and the Legendre coefficients show that $\delta r_{T,p}$ and $\delta r_{\rho,p}$ are of the order of a few meters for this model. A similar result would be found for other models that use a reasonable rotation curve. This implies, to a very good approximation, that surfaces of constant P, ρ and T all coincide for a rotational perturbation and are related to a surface of constant gravitational potential by equation 2.2.11.

REFERENCES

- Anderson, B.N., and Maltby, P. 1983, *Nature*, 302, 808.
- Bohm-Vitense, E. 1955, *Z. Astrophys.*, 36, 145.
- Bos, R. J., 1982, "Observations of Individual Solar Eigenmodes: Their Properties and Implications," Ph. D. Thesis, University of Arizona.
- Brans, C. and Dicke, R. H., 1961, *Phys. Rev.*, 124, 925.
- Brown, T.M. 1985, *Nature*, 317, 591.
- Chapman, G. A. and Ingersoll, A. P., 1972, *Ap. J.*, 175, 819.
- Chapman, G. A. and Klabunde, D. P., 1982, *Ap. J.*, 261, 387.
- Claverie, A., Isaak, G. R., McLeod, C. P., Van der Raay, H. B., Palle, P.L., and Roca Cortes, T., 1982, *Nature*, 299, 704.
- Clayton, P.D., 1973, "A Precise Measurement of the Sun's Visual Oblateness," Ph. D. Thesis, University of Arizona, Tucson Az.
- Delache, P., and Scherrer, P., 1983, *Nature*, 306, 651.
- Dicke, R. H., 1970, *Ap. J.*, 159, 1.
- Dicke, R. H., 1976, *Solar Phys.*, 47, 475.
- Dicke, R. H., 1977 *Ap. J.*, 218, 547.
- Dicke, R. H., 1981, *Proc. Natl. Acad. Sci.*, 78, 1309.
- Dicke, R. H., 1982, *Solar Phys.*, 78, 3.
- Dicke, R. H., 1983, *Nature*, 303, 292.
- Dicke, R. H. and Goldenberg, H. M., 1967, *Phys. Rev. Lett.*, 18, 313.
- Dicke, R. H. and Goldenberg, H. M., 1974, *Ap. J. Suppl.*, 27, 131.
- Dicke, R. H., Kuhn, J. R. and Libbrecht, K. G., 1985, *Nature*, 316, 687.
- Dicke, R. H., Kuhn, J. R. and Libbrecht, K. G., 1986, *Ap. J.*, 311, 1025.

- Durney, B. R., 1973, Ap. J., 183, 665.
- Durney, B. R. and Roxburgh, I. W., 1969, Nature, 221, 646.
- Durney, B. R. and Werner, N. E., 1971, Solar Phys., 21, 21.
- Duvall, T. L. and Harvey, J. W., 1983, Nature, 302, 24.
- Duvall, T. L., Harvey, J. W. and Pomerantz, M. A., 1986, Nature, 321, 500.
- Dziembowski, W. and Goode, P. R., 1983, Nature, 305, 39.
- Einstein A., 1916, "Näherungsweise Integration der Feldgleichungen der Gravitation," Preuss. Akad. Wiss. Berlin Sitzber. Pg. 688-696.
- Hill, H. A., 1984, SCLERA Monograph Series in Astrophysics, No. 1.
- Hill, H. A., 1985a, Ap. J., 290, 765.
- Hill, H. A., 1985b, SCLERA Monograph Series in Astrophysics, No. 3.
- Hill, H. A., 1986, SCLERA Monograph Series in Astrophysics No. 4.
- Hill, H. A., Alexander, N., and Caudell, T. P., 1987, SCLERA Monograph Series in Astrophysics, No. 2.
- Hill, H. A. and Beardsley, B. J., 1987, SCLERA Monograph Series in Astrophysics, No. 7.
- Hill, H. A., Bos, R. S. and Goode, P. R., 1982, Phys. Rev. Lett., 49, 1794.
- Hill, H. A. and Czarnowski, W. M. 1986, SCLERA Monograph Series in Astrophysics, No. 6.
- Hill, H. A., Rabaey, G. R. and Rosenwald, R. D. 1986, "Relativity in Celestial Mechanics and Astrometry," IAU Symposium No. 114, eds. J. Kovalesky and V. A. Brumberg, (Reidel) 345.
- Hill, H. A., Rabaey, G. R., Yakowitz, D. and Rosenwald, R. D. ,1986, Ap. J., 310, 444.
- Hill, H. A. and Rosenwald, R. 1986, Proceedings of the NATO Advanced Workshop, "Mathematical Aspects of Gravity and Supergravity.
- Hill, H. A. and Stebbins, R. T., 1975a, Ap. J., 200, 471.
- Hill, H. A. and Stebbins, R. T., 1975b, Ann. of N. Y. Acad. of Sci., 262, 472.

- Hill, H. A., Stebbins, R. T., and Brown, T. M. 1976, Masses and Fundamental Constants, 5, 622.
- Hill, H. A., Stebbins, R. T. and Oleson, J. R., 1975, Ap. J., 200, 484.
- Ingersoll, A. P., and Spiegel, E. A., 1971, Ap. J., 163, 375.
- Kotov, V. A., Severny, A. B., Tsap, T. T., Moiseev, I. G., Efanov, V. A. and Nesterov, N. S., 1983, Solar Phys., 82, 9.
- Libbrecht, K. G., 1984, "The Shape of the Sun," Ph. D. Thesis, Princeton University.
- Libbrecht, K. G. and Zirin, H., 1986, Ap. J., 308, 413.
- Oleson, J. R., Zanoni, C. A., Hill, H. A., Healy, A. W., Clayton, P. D., and Patz, D. L., 1974, Appl. Opt., 13, 206.
- Patz, D. L., 1975, "An Experimental Method to Determine Small Differences Between the Poles and Equatorial Solar Limb Profiles," Ph. D. Thesis, University of Arizona.
- Shapiro, I. I., Counselman, C. C. III., and King, R. W., 1976, Phys. Rev. Lett., 36, 555.
- Smart, W. M. 1977, "Textbook on Spherical Astrometry," Cambridge University Press.
- Snodgrass, H. B., 1983, Ap. J., 270, 288.
- Stebbins, R. T., 1975, "An Observational Investigation of the Solar Oblateness," Ph. D. Thesis, University of Colorado, Boulder Colorado.
- Ulrich, R. K. and Hawkins, G. W., 1981, Ap. J., 246, 985.
- Unno, W., Osaki, Y., Ando, H. and Shibahashi, H., 1979, "Non Radial Oscillations of Stars," pg. 78, University of Tokyo Press.
- Vernazza, J. E., Avrett, E. H., and Loesser, R., 1976, Ap. J. Suppl., 30, 1.
- Von Zeipel, H., 1924, M.N.R.A.S., 84, 665.
- Will, C. A., 1981, "Theory and Experiment in Gravitational Physics," Cambridge University Press.
- Will, C. A. 1984, Phys. Reports Vol. 113, No. 6, 347.

Will, C. A. 1986, "Relativity in Celestial Mechanics and Astrometry, IAU Symposium No. 114, eds. J. Kovalesky and V. A. Brumberg, (Reidel) pg. 355.

Zanoni, C. a., 1966, "Development of Daytime Astrometry to Measure the Gravitational Deflection of Light," Ph. D. Thesis, Princeton University.